Güdel et al. 1996; Osten et al. 2004).

Observations of magnetic activity tracers in UCDs paint a different picture. Despite the demonstrated existence of strong fields in at least some UCDs, their X-ray and Hα emission both drop off precipitously (Stelzer et al. 2006a; Berger et al. 2010; Gizis et al. 2000; West et al. 2004). The rotation/activity relation evolves significantly in UCDs, with evidence of X-ray and Hα "supersaturation" trends in which activity decreases as rotation increases (Basri & Marcy 1995; Mohanty & Basri 2003; West & Basri 2009; Berger et al. 2010). But UCD radio emission remains stubbornly unchanged: in this regime, radio activity and radio surface flux ($L_{\rm rad}/R_*^2$) increase with rotation, with no evidence of saturation (McLean et al. 2012).

These trends offer clues toward a deeper understanding of the fully convective dynamo and the structures of (sub)stellar magnetic fields and outer atmospheres. Progress toward this understanding, however, is hampered by the relatively small number of UCDs detected in the X-ray regime. In an attempt to improve this situation, we have observed numerous UCDs with the *Chandra* X-ray Observatory (Berger et al. 2005, 2008a,b, 2009, 2010). In this work, we report new *Chandra* observations of 7 UCDs of spectral type ∼M7 with a wide range of rotational velocities, all of which were detected. Every source was also observed (non-simultaneously) with the upgraded Karl G. Jansky Very Large Array (VLA), yielding one detection. Our *Chandra* detections offer a striking counterpoint to previous observations of later-type objects, in which X-ray detections were elusive. We also report the analysis of several unpublished measurements from archival data. We combine these results with data from our previous work and the literature to form a comprehensive database of UCD activity measurements.

In this work, we use this database to investigate the correlation between X-ray and radio emission in UCDs. We proceed here by describing the targets for which we present new results (§2) and our data analysis (§§3, 4). We then discuss our results in the context of the full sample of UCDs with X-ray and radio observations (§5). We offer a physical model that explains the observations (§6). In Cook et al. (2013, hereafter Paper II), we use the same database to investigate the correlation between UCD X-ray emission and rotation.

Throughout this work, we use the notation $[x] \equiv \log_{10} x$, with x being measured in cgs units if it is a dimensional quantity, unless its units are specified otherwise.

2. TARGETS WITH NEW RESULTS

Candidates for new radio and X-ray observations were selected by searching dwarfarchives.org for nearby UCDs of spectral type ∼M7 that were visible to the VLA and had measurements of $v \sin i$ in the literature. We also searched the *Chandra* data archive for unpublished observations of late-type objects with $v \sin i$ measurements. Seven targets were observed with *Chandra* and the VLA, and we identified and analyzed four archival targets. The main characteristics of these objects, along with the appropriate references and 2MASS identifications (Skrutskie et al. 2006), are provided in Table 1, while their properties are discussed in greater detail in the Appendix. The Appendix also describes our method for computing bolometric luminosities.

2.1. *Observations*

The new observations were performed with *Chandra*/ACIS-S between 2011 December and 2013 February (proposal 13200167; *Chandra* observation IDs 13603–13609; PI: Berger), using the S3 backside-illuminated chip. All exposures were 20 ks, except for LHS 292 which was observed for 10 ks. Parameters of the observations are provided in Table 2. No grating was used, the data mode was VFAINT, and the exposure mode was "timed" (TE).

The targets were also observed with the Karl G. Jansky Very Large Array (VLA) between 2012 February and 2012 May (project VLA/12A-089; PI: Berger). These observations were not simultaneous with the X-ray observations, and the relative timing between observations in the two bands was arbitrary. Each observing session lasted 1 hr, with a total correlated bandwidth of 2048 MHz divided into two basebands centered at 5000 and 7100 MHz, each containing 512 spectral channels. Bandpass, flux density scale, and complex gain calibrations were obtained in the usual way; the sources used are listed in Table 3, along with other parameters of the observations. Approximately 65% of each session was spent integrating on the target source.

The archival data were obtained as follows. G 208-44AB/45 was observed with *Chandra*/ACIS-S on 2003 December 14 (proposal 05200058; *Chandra* observation ID 4476; PI: Garmire) for 24 ks. DENIS 0255−4700 was observed in two parts (proposal 09200200; observation IDs 8903 and 10828; PI: Audard) on 2008 December 2 and 2008 December 4, for a total exposure time of 28 ks. LP 349–25 AB was observed on 2009 September 15 (proposal 10200468; observation ID 9925; PI: Osten) with an exposure time of 37 ks. In all cases, the instrumental configuration was the same as in our new observations.

3. X-RAY ANALYSIS

We analyzed the *Chandra* data in CIAO version 4.5 (Fruscione et al. 2006) with CalDB version 4.5.5.1. We used the date of each observation and astrometric information from the Simbad database to predict positions for each target at the time of our observations. Based on Monte Carlo simulations, all of our predictions have uncertainties of $\lesssim 2''$, and most of them have uncertainties of $\lesssim 0.5''$. This is comparable to the astrometric precision of *Chandra*. We defined initial source apertures $2''$ in radius centered on our astrometric predictions of the source positions. As discussed below, two of our targets (G 208–44 AB and G 208–45) are affected by pileup, leading us to use annular apertures instead. For the rest of the targets, the initial apertures needed no modification.

Following VFAINT reprocessing to eliminate a substantial fraction of the background events, we estimated the mean residual background in each dataset by extracting events in an energy range of 0.3–7 keV in large, source-free regions near the target locations. In all cases, the expected number of background counts in the source aperture is $\lesssim 1$.

Every source except the archival L8 dwarf DENIS 0255−4700 was detected at $>5\sigma$ significance. In our new observations, the number of counts at the source location ranges between 6 (NLTT 40026, with 0.17 expected background events) and 252 (LHS 2397a AB). With the high success rate in our new observations, we nearly

Table 1
Properties of Ultracool Dwarfs with New Analysis Presented in This Paper

2MASS Identifier	Name	Distance (pc)	SpT	$v \sin i$ (km s^{-1})	References					
					(P)	(C)	(M)	(D)	(S)	(V)
(1)	(2)	(3)	(4)	(5)						
Newly-observed targets										
01095117−0343264	LP 647−13[a]	11.1 $\pm^{0.6}_{0.7}$	M9	13 ± 2	1	2		3	3	4
10481258−1120082	LHS 292	4.54 $\pm$ 0.07	M6.5	<3	5	6		8	7	4
11214924−1313084 A	LHS 2397a A	14.3 $\pm$ 0.4	M8	15 ± 1	5	9	10	8	10	11
B	B		L7.5	11 ± 3					10	11
11554286−2224586	LP 851−346	9.6 $\pm$ 1.0	M7.5	33 ± 3	5	12		13	13	4
15210103+5053230	NLTT 40026	16 ± 2	M7.5	40 ± 4	1	3		3	3	4
18432213+4040209	LHS 3406	14.13 $\pm^{0.20}_{0.10}$	M8	5 ± 3.2	5	14		8	3	4
22285440−1325178	LHS 523	11.3 $\pm$ 0.6	M6.5	7.0 ± 2	5	15		8	16	17
Chandra archival targets										
00275592+2219328 A	LP 349−25 A	13.2 $\pm$ 0.3	M8	55 ± 2	5	18	19	20	19	11
B	B		M9	83 ± 3					19	11
02550357−4700509	DENIS 0255−4700	4.96 $\pm^{0.10}_{0.09}$	L8	67 ± 13	21	22		23	3	24
19535443+4424541 A	G 208−44 A	4.61 $\pm$ 0.04	M5.0	22.5 ± 2	5	25	26	28	27	17
B	B		M8.5	17.4 ± 1.4[b]	5	29			27	28
19535508+4424550	G 208−45		M5.5	6.8 ± 1.9	5	25			14	28

References. — Columns are (P), discovery of substantial proper motion; (C), classification as very cool dwarf; (M), discovery of multiplicity; (S), spectral type; (D), distance; (V), $v \sin i$. [1] Luyten (1979), [2] Cruz & Reid (2002), [3] Cruz et al. (2003), [4] Reiners & Basri (2010), [5] Luyten (1976), [6] Dahn et al. (1986), [7] Henry et al. (1994), [8] van Altena et al. (1995), [9] Gliese & Jahreiß (1991), [10] Freed et al. (2003), [11] Konopacky et al. (2012), [12] Phan-Bao et al. (2003), [13] Crifo et al. (2005), [14] Reid et al. (1995), [15] Liebert et al. (1979), [16] Kirkpatrick et al. (1991), [17] Mohanty & Basri (2003), [18] Gizis et al. (2000), [19] Forveille et al. (2005), [20] Gatewood & Coban (2009), [21] Casewell et al. (2008), [22] Martín et al. (1999), [23] Costa et al. (2006), [24] Reiners & Basri (2008), [25] Harrington et al. (1974), [26] Harrington & Dahn (1984), [27] Law et al. (2008), [28] Delfosse et al. (1998), [29] McCarthy et al. (1988)

Note. — See Appendix for additional details and references.
[a] Possible binary; see Guenther & Wuchterl (2003).
[b] Measurement is a blend of both system components.

double the number of UCDs with X-ray detections (cf. Table 6). The only target with nontrivial X-ray structure and annular source extraction apertures, the triple system G 208-44AB/45, is shown in Figure 1. Cutouts of the X-ray images around the predicted locations of the other sources (as well as radio images; see next section) are shown in Figure 2.

During extraction we also checked for background flaring. The only dataset in which flares were seen was the observation of G 208-44AB/45. We discuss our handling of this dataset separately below.

We searched for variability in the X-ray emission of the detected sources using a Bayesian blocks analysis (Scargle 1998; Scargle et al. 2013). This approach models the source flux as a series of independent, piecewise constant "blocks," with overfitting being controlled by the use of a downward-sloping prior on the number of blocks (N_b). Our implementation of the algorithm uses the iterative approach described in Scargle et al. (2013) with a Monte-Carlo-derived parametrization of the prior on N_b that sets the probability of false detection of an extraneous block at 5%. This parametrization is given in Equation 21 of Scargle et al. (2013) but is misstated; the correct equation is

$$\mathrm{ncp\_prior} = 4 - \ln\left(73.53 p_0 N^{-0.478}\right), \qquad (1)$$
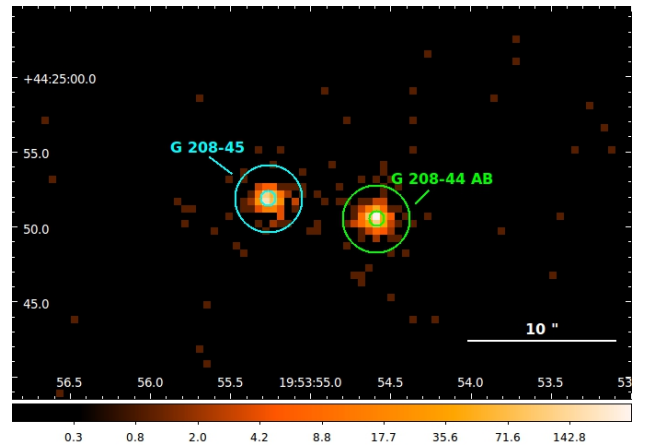

Figure 1. Annotated *Chandra* image cutout of the G 208-44AB/45 system. This image was generated after filtering out periods of background flaring as described in §3.2. G 208–45 is to the east (left) and the unresolved pair G 208–44 AB is to the west (right). The annuli around each object represent the areas from which counts were extracted to avoid pileup in the central pixels (§3.2). A colorbar below indicates the scale, which is in terms of total counts accumulated over the unfiltered intervals of the observation.

as may be verified with the example given in that work. Our implementation is in Python and derives from the MatLab$^{\mathrm{TM}}$ code provided by Scargle et al. (2013) and

Table 2
Parameters of *Chandra* Observations

Name	Observation Date		ObsId	Integ. Time (s)	Raw Counts
	Gregorian	MJD[TT]			
(1)	(2)	(3)	(4)	(5)	(6)
Newly-observed targets					
LHS 292	2011 Dec 14	55909.56	13603	10620	51
LHS 523	2012 Dec 08	56269.18	13604	19605	15
LHS 2397a AB	2012 Nov 05	56236.01	13606	19804	252
LHS 3406	2012 Dec 05	56266.17	13609	19804	74
LP 647–13	2012 Oct 24	56224.21	13605	19798	12
LP 851–346	2012 Jul 09	56117.63	13607	19800	43
NLTT 40026	2013 Feb 07	56330.68	13608	18812	6
Chandra archival targets					
G 208–44 AB	2003 Dec 14	52987.18	4476	23785[a]	1607[b]
G 208–45	2003 Dec 14	52987.18	4476	23785[a]	1072[b]
DENIS 0255−4700	2008 Dec 02	54802.28	8903	17993	0
DENIS 0255−4700	2008 Dec 04	54804.79	10828	9914	1
LP 349–25 AB	2009 Sep 15	55089.28	9225	37197	60

Note. — Cols. (2) and (3) are the approximate midpoint of the on-source integration. Col. (4) is the *Chandra* observation ID. Col. (5) is the on-source integration time, not accounting for the background flares described in the text. Col. (6) is the number of counts in a $2''$ aperture around the predicted source position after processing in the VFAINT background mode, not accounting for pileup.
[a] Affected by background flaring (see §3).
[b] Affected by pileup (see §3).

Table 3
Parameters of VLA Observations

Name	Observation Date		Integ. Time (s)	Config.	Flux Cal.	Gain Cal.
	Gregorian	MJD[TT]				
(1)	(2)	(3)	(4)	(5)	(6)	(7)
LHS 292	2012 Feb 22	55979.24	2260	C	3C 286	J1039−1541
LHS 523	2012 Mar 17	56003.76	2205	C	3C 48	J2246−1206
LHS 523	2012 May 21	56068.50	2200	CnB	3C 48	J2246−1206
LHS 2397a AB	2012 Feb 22	55979.36	2335	C	3C 286	J1130−1449
LHS 3406	2012 Mar 17	56003.71	2205	C	3C 48	J1845+4007
LP 647–13	2012 Feb 22	55979.04	2265	C	3C 48	J0110−0741
LP 851–346	2012 Feb 28	55985.27	2205	C	3C 286	J1159−2148
NLTT 40026	2012 Mar 16	56002.54	2205	C	3C 286	J1545+5135

Note. — LHS 523 was observed twice. Cols. (2) and (3) are the approximate midpoint of the on-source integration. Col. (4) is the on-source integration time. Col. (5) is the configuration of the VLA at the time of the observation.

the AstroML Python module (VanderPlas et al. 2012). Compared to the latter module, our system adds support for time-tagged events and datasets with gaps in coverage (due to the background flaring in our case). It also fixes several minor bugs such as the mistaken equation above. Our implementation is publicly available[3].

The Bayesian blocks analysis finds more than one block — that is, significant evidence of variability — in five sources. We plot the X-ray light curves resulting from this analysis in Figure 3, also showing the results of uniform binning for reference. The plots also indicate the "good time intervals" in which background flares were not an issue; they are continuous except for the observations

of G 208-44AB/45. Table 4 includes information on the flare durations and fluxes. Of the five sources with more than one block, four of them contain two blocks, suggesting partially-observed flares. The last, LP 851–346, has three blocks, with the pre- and post-flare fluxes agreeing at the ∼20% level. From visual inspection of Figure 3, one may conclude that both a flatter prior on N_b (i.e., an assumption of a higher likelihood that sources are variable) and that a non-piecewise-constant emission model would lead to more faithful approximations of the data. Because the aim of our analysis is limited to identifying representative quiescent and (when appropriate) flaring X-ray fluxes, we do not explore these possible elaborations here.

We determined X-ray fluxes in the 0.2–2 keV band using either spectral modeling or a simple energy conversion factor (ECF). We used the ECF approach for all but the three brightest sources: LHS 2397a AB, G 208–44 AB, and G 208–45. After extracting spectra from the event data

---

[3] The implementation is versioned using Git and is currently available at https://github.com/pkgw/pwpy/blob/master/scilib/xbblocks.py. The version used in this work is that included in commit 606218c47d667e97d58c38f1fd09e7dc5540b38f. The design of Git ensures that this commit identifier uniquely specifies the exact content and complete revision history of the code in question.
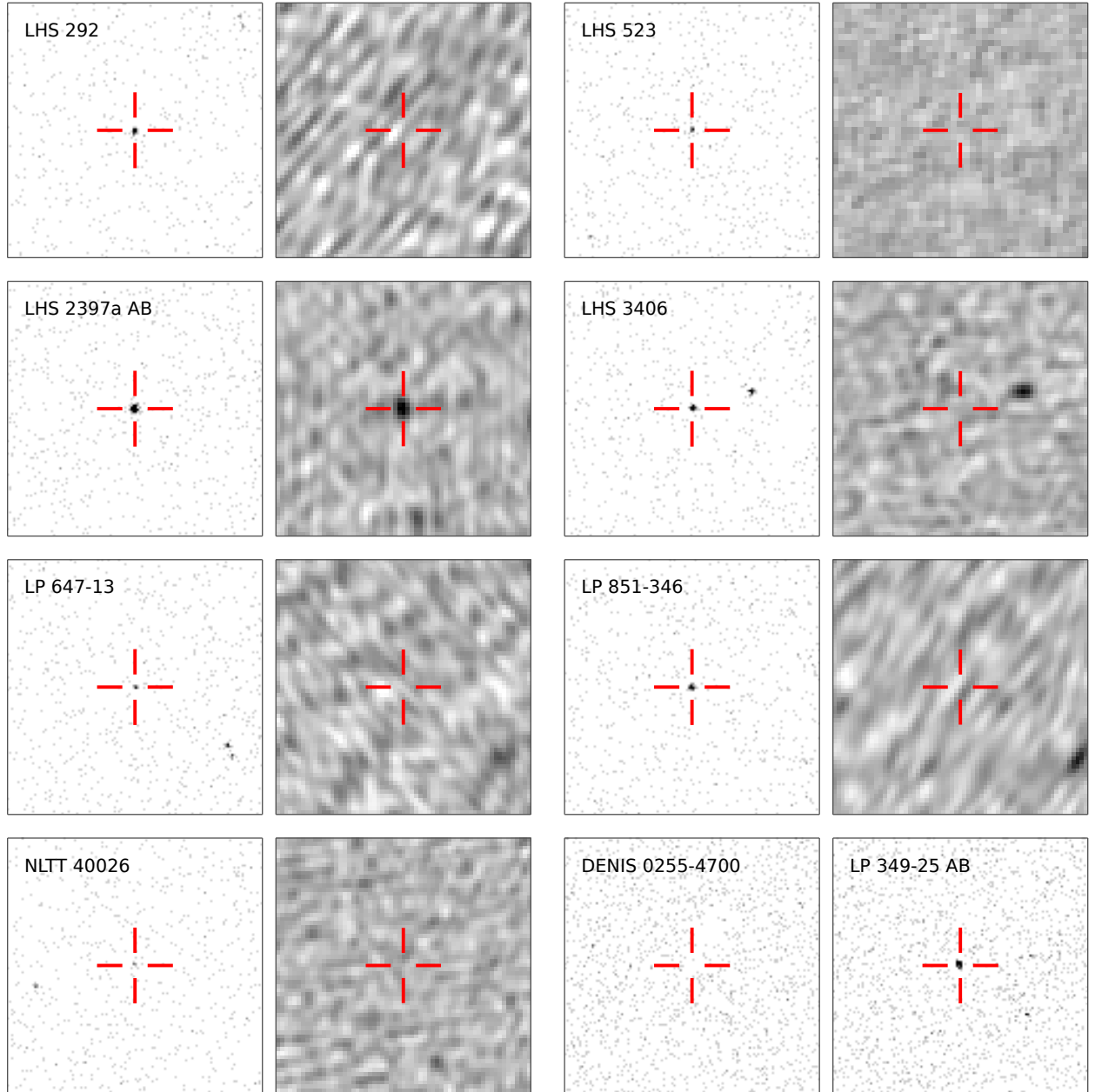
Figure 2. X-ray and radio image cutouts of all sources except G 208-44AB/45 (Figure 1). Each panel is $1' \times 1'$. In each pair of panels except the last, the left-hand panel shows X-ray counts after **VFAINT** background processing on a white-to-black linear scale ranging from 0 to 10 counts. The right-hand panels show radio brightness on a white-to-black linear scale ranging from -20 to 50 μJy bm^{-1}. Radio results from the literature were used for DENIS 0255−4700 and LP 349−25 AB, which are shown as the bottom-right pair of panels. The radio/X-ray source near the predicted position of LHS 3406 is discussed in §4. Note also the plausible joint radio/X-ray detections of unrelated sources within the cutouts of LP 647–13 (36 X-ray counts, combining the resolved pair; $S_{\nu,\mathrm{max}} \approx 28$ μJy bm^{-1}) and LP 851–346 (4 counts within a $1''$ aperture; $S_{\nu,\mathrm{max}} \approx 43$ μJy bm^{-1}).

of these three sources, grouping into bins of ≥ 12 events, we used **Sherpa** version 1 (Freeman et al. 2001) for the modeling, ignoring energies outside of the standard ACIS energy filter of 0.3–7 keV. We used the **Sherpa** implementation of the Nelder & Mead (1965) simplex algorithm to optimize the modified χ^2 statistic of Gehrels (1986). Solar abundances were taken from Lodders (2003). Our X-ray flux results and the outcomes of the modeling are discussed below. We summarize the fluxes in Table 4, where the uncertainties are properly propagated and account for Poisson statistics as appropriate. Derived quantities

for the UCDs, including X-ray luminosities, are presented in Table 8.

3.1. *LHS 2397a AB*

In LHS 2397a AB, a one-temperature, solar-abundance APEC (Astrophysical Plasma Emission Code; Smith et al. 2001) model yields a satisfactory fit, achieving a reduced statistic $\chi_r^2 = 1.1$ with 18 degrees of freedom (DOF), although there are strong correlations among the residuals. The data and best-fit model are shown in Figure 4.

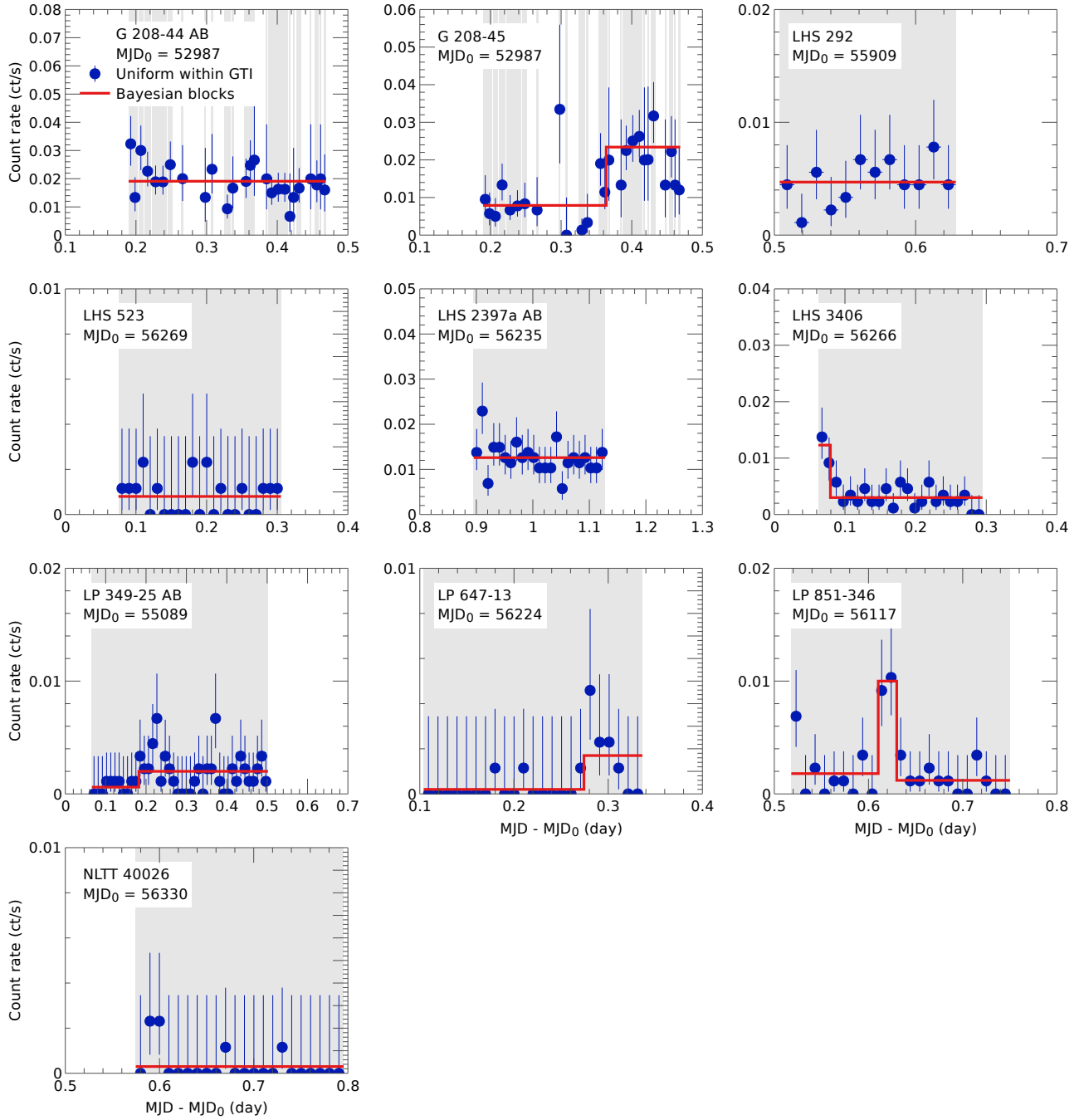The model-fitting procedure finds $kT = 0.78 \pm 0.04$ keV,

Figure 3. Light curves of the detected *Chandra* targets in the 0.3–7 keV energy range. Note the differing axis ranges for each panel. *Shaded regions* indicate "good times" in which background flares are not dominant (§3.2). *Blue points* give count rates derived from bins that are uniformly-sized within each good time interval, with error bars from Poisson statistics. *Red histograms* give the piecewise constant model derived from Bayesian block variability analysis (§3).

but we caution generally against overinterpreting the parameters derived from our spectral fits. While the data we present cannot rule out a single-temperature solar-abundance model, the truth is likely more complicated. In particular, the value of kT we report above is quite possibly an approximate average of multiple temperature components. Intriguingly, if we overfit the data by adopting a two-temperature model, we find temperatures of ~0.3 and ~1.2 keV, in good agreement with other results from mid-to-late M dwarfs (e.g., Robrade & Schmitt 2005). Similarly, if we use a single-temperature model

with variable abundances, the fits tend to converge on an inverse first ionization potential (FIP) effect, with higher abundances found for elements with higher FIPs, as is commonly seen in higher-S/N spectra of similar objects (e.g., Robrade & Schmitt 2005). We emphasize, however, that these findings are not statistically significant.

Granting these caveats, the fluxes we derive from our spectral modeling are robust, because the essential shapes of the X-ray spectra are well-constrained by the data. For LHS 2397a AB we find the X-ray flux in the 0.2–2 keV band to be $[f_X] = -13.29 \pm 0.04$. At our adopted

Table 4
Results of *Chandra* Analysis

Name	State	Integ. Time (s)	Counts	$[f_X]$ [erg s^{-1} cm^{-2}]
(1)	(2)	(3)	(4)	(5)
Newly-observed targets				
LHS 292	M	10620	51	-13.7 ± 0.1
LHS 523	M	19605	15	-14.5 ± 0.1
LHS 2397a AB	M	19804	252	-13.29 ± 0.04
LHS 3406	M	19804	74	-13.8 ± 0.1
	Q	17342	56	-13.9 ± 0.1
	F	2462	18	-13.3 ± 0.1
LP 647–13	M	19798	12	-14.6 ± 0.2
	Q	14504	3	-15.0 ± 0.2
	F	5294	9	-14.1 ± 0.2
LP 851–346	M	19800	43	-14.0 ± 0.1
	Q	18126	26	-14.2 ± 0.1
	F	1675	17	-13.3 ± 0.1
NLTT 40026	M	18812	6	-14.8 ± 0.2
Chandra archival targets				
G 208–44 AB	M	12089	234	$-13.05 \pm^{0.04}_{0.05}$
G 208–45	M	12089	170	$-13.22 \pm^{0.07}_{0.08}$
	Q	7459	60	-13.4 ± 0.1
	F	4630	110	-13.0 ± 0.1
DENIS 0255−4700	M	27908	1	< -15.2
LP 349–25 AB	M	37197	60	-14.1 ± 0.1
	Q	9926	6	-14.5 ± 0.2
	F	27270	54	-14.0 ± 0.1

Note. — Col. (2) is the source state, one of mean (M), quiescent (Q), or flaring (F). Col. (3) is the integration time after background flares have been removed. Col. (4) is counts in the final apertures, accounting for the flagging of periods of background flaring and removal of piled-up pixels. Col. (5) is the X-ray flux in the 0.2–2 keV band.

distance, this corresponds to $[L_X] = 27.1$ and $[L_X/L_{bol}] = -3.1$, near the canonical "saturation" value of the X-ray/rotation activity relation observed in solar-type stars (e.g., Pizzolato et al. 2003).

3.2. *G 208-44AB/45*

While G 208–44 AB and G 208–45 are clearly resolved in the *Chandra* image (Figure 1), the tighter binary (G 208–44 A and B) is not. The following analysis considers only the blended emission of G 208–44 AB.

During our analysis of the G 208-44AB/45 dataset, we discovered significant background flaring activity. We used standard CIAO tools to extract a light curve of non-source regions on the source chip (S3), binning by 150 s in time and finding a non-flaring background rate of 0.32 s^{-1} across the whole chip, which is consistent with typical nonflaring behavior. We flagged bins in which the measured background rate varied from this value by $>4\sigma$. After processing, the good exposure time was reduced from 23.8 to 12.1 ks. We note that the Bayesian blocks method can be applied to data with observational gaps without adjustment (Scargle et al. 2013), making it

well-suited for these data.

Both components of the system additionally achieved count rates sufficiently high (>0.1 s^{-1}) to make pileup a concern. We used the Portable, Interactive Multi-Mission Simulator (PIMMS) to estimate the pileup percentages during the observations. For both objects, pileup was estimated at the ∼5% level. To compensate for this we analyzed both components using annuli centered on the source positions, removing the centermost pixels where the count rate and hence pileup were greatest. For both sources, the annuli had inner (outer) radii of 0.5 (2.25) arcsec. This approach discards significant signal, but both sources were bright enough that we still retained strong detections sufficient for spectral modeling. The reported fluxes account for the reduced portion of the PSF being sampled. Filtering of background flares and removal of the central pixels reduced the number of counts detected at the position of G 208–44 AB from 1607 to 234; for G 208–45, the numbers are 1072 and 170, respectively.

In G 208–44 AB, the Bayesian blocks analysis detects no significant variability, and a one-temperature, solar-abundance APEC model yields a satisfactory fit, achieving
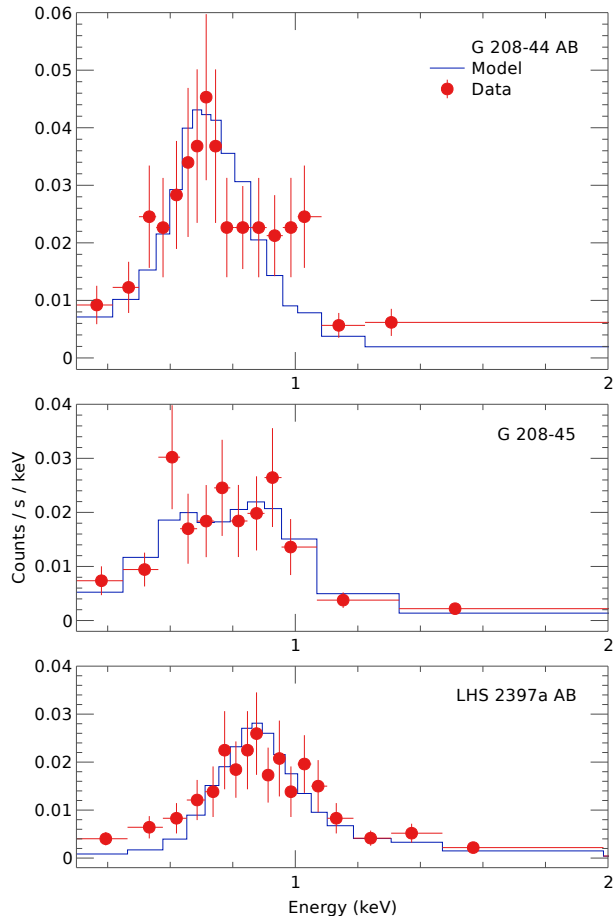
Figure 4. Mean X-ray spectra of G 208–44 AB, G 208–45, and LHS 2397a AB (*red*) and best-fit spectral models (*blue*). The horizontal lines associated with each data point indicate bin widths. G 208–44 AB is modeled as a 0.30 keV plasma, G 208–45 as two-temperature plasma with $kT_1 = 0.22$ keV and $kT_2 = 0.87$ keV, and LHS 2397a AB as a 0.78 keV plasma. See text for caveats on the details of the model results.

$\chi_r^2 = 1.2$ with 16 DOF. In this case as well there are strong correlations among the residuals. The best-fit temperature in the adopted model is $kT = 0.30 \pm 0.02$ keV, subject to the same caveats mentioned above. We find $[f_X] = -13.05_{-0.05}^{+0.04}$ (0.2–2 keV). At our adopted distance, $[L_X] = 26.4$ and $[L_X/L_{bol}] = -4.49$.

In G 208–45, the Bayesian blocks analysis finds that the count rate in the final 9 ks of the observation is elevated by a factor of ~3. Although flaring is often associated with spectral variability (e.g., Osten et al. 2005), there were few enough counts available that we chose to only model the mean spectrum of the source. We found that a one-temperature, solar-abundance model yielded a less satisfactory fit, with $\chi_r^2 = 2.0$ for 11 DOF. A two-temperature, solar-abundance model yields $\chi_r^2 = 0.8$ (9 DOF) with $kT_1 = 0.22 \pm 0.5$ keV and $kT_2 = 0.87 \pm 0.14$ keV. We find $[f_X] = -13.22_{-0.08}^{+0.07}$ (0.2–2 keV), $[L_X] = 26.2$, and $[L_X/L_{bol}] = -4.48$. For comparison, a one-temperature fit with variable abundance finds $\chi_r^2 = 1.2$ (10 DOF), $kT = 0.59_{-0.15}^{+0.10}$ keV, $Z/Z_\odot = 0.08_{-0.03}^{+0.05}$, and $[f_X] = -13.35 \pm 0.35$. Despite their differences, the two models yield values of f_X that agree within their uncertainties.

3.2.1. *Did ROSAT observe G 208-44AB/45 during a flare?*

Previous X-ray observations of the G 208-44AB/45 system were performed as part of the *ROSAT* All-Sky Survey (RASS), with follow-up on the *ROSAT* High Resolution Imager (HRI). While the latter was capable of resolving the triple system into its two main components (resolution ~2″; separation ~7″), the former, with a resolution of ~5–10′ (Voges et al. 1999), was not. While Schmitt & Liefke (2004) correctly identify the ROSAT source as the blend of all three components, we note that Law et al. (2008) failed to highlight this in their summary of the X-ray properties of G 208–44 AB.

The RASS catalog luminosity for G 208-44AB/45 is $[L_X] = 27.47$ in the 0.1–2.4 keV band. After correction to the ROSAT bandpass, this exceeds the sum of our resolved measurements by a factor of ~6. This suggests that the RASS observations of G 208-44AB/45 may have occurred during a strong flare. The RASS exposure time during the observation was 730 s (Schmitt & Liefke 2004), shorter than the typical timescale of such events. The later *ROSAT* HRI measurements find $[L_X] = 27.19$ with an integration time of 2849 seconds (Schmitt & Liefke 2004), in better agreement with the *Chandra* results, though still exceeding them by a factor of ~2. As X-ray flares may easily result in luminosity increases of an order of magnitude (cf. Figure 5), it would not take an unusually large flare to reconcile the two measurements. On the other hand, the fact that both *ROSAT* measurements exceed the combined *Chandra* flaring luminosity, despite their separation in time (8 months), suggests that perhaps the X-ray activity of this system has decreased since the time of the RASS, possibly due to a long-term magnetic activity cycle (e.g., Baliunas et al. 1996).

3.3. *Other Detected Sources*

We determined X-ray fluxes for the other detected sources by assuming an energy conversion factor (ECF) of $(4.5 \pm 1) \times 10^{-12}$ erg cm^{-2} count^{-1}, where the uncertainty approximately accounts for the range of plasma temperatures and abundances commonly encountered. The applicable theoretical ECF reported by WebPIMMS version 4.6a for a 0.5 keV APEC plasma with $Z/Z_\odot = 0.6$ is 4.4×10^{-12} erg cm^{-2} count^{-1}. Our adopted value agrees with those derived for LHS 2397a AB, G 208–44 AB, and G 208–45 (ECF = $(4.3, 4.6, 4.3) \times 10^{-12}$, respectively) as well as our previous observations of X-ray-emitting UCDs (Berger et al. 2008a,b). Spectral modeling of the other sources with larger numbers of events (LHS 292, LHS 3406, LP 851–346) yields results consistent with those reported here.

3.4. *Undetected Source: DENIS 0255−4700*

Only one photon in the 0.3–7 keV range was detected at the predicted location of DENIS 0255−4700 throughout both observations, compared to the expected background level of 0.7 counts in 28 ks. The resulting 95% confidence upper limit is 4.3 counts (Kraft et al. 1991). Using the above energy conversion factor, the time-averaged flux limit is $[f_X] < -15.2$. At our adopted distance of 5.0 pc, we can thus constrain the persistent emission of DENIS 0255−4700 to be $[L_X] \lesssim 24.3$, or $[L_X/L_{bol}] \lesssim -4.70$.

4. RADIO ANALYSIS

We calibrated the VLA using standard procedures in the CASA software system (McMullin et al. 2007). Radio-frequency interference was flagged automatically using the aoflagger tool, which provides post-correlation (Offringa et al. 2010) and morphological (Offringa et al. 2012) algorithms for identifying interference. At the time of analysis, aoflagger did not include a set of tuning parameters suitable for the processing of VLA data, so these were developed manually.

We created deep Stokes I images of each field with 2048×2048 pixels, each 1×1 arcsec², except the image of LHS 523, for which a pixel scale of 1.5×1.5 arcsec² was used to include the nearby, bright blazar QSO B2227−136 in the image. The imaging process used multi-frequency synthesis (Sault & Wieringa 1994) and CASA's multi-frequency CLEAN algorithm with 1500 iterations. Two spectral Taylor series terms were used for each CLEAN component; this approach models both the flux and spectral index of each source. The reference frequency for each image is 6.05 GHz. Properties of the images are listed in Table 5. Astrometric predictions of the source locations were computed as described above, and cutouts of the VLA images around the predicted source locations are show in Figure 2. The accuracy of VLA astrometry in our observing configuration is ∼1″, comparable to that of our predictions. While our targets have relatively high proper motions, the time baseline between the pairs of VLA and *Chandra* observations is sufficiently small that the differences in the predicted positions are negligible.

We detect a radio source in the image of the LHS 2397a AB field at position RA = 11:21:48.78, Dec = −13:13:09.4, coincident with our astrometric prediction of RA = 11:21:48.77, Dec = −13:13:09.5. We re-imaged this field, rephasing the data to place this position on a pixel center to obtain the most accurate source parameters from image-domain modeling. Fitting the rephased image with a point-source model yields a flux density of 63 ± 7 μJy and a positional uncertainty of 0.4″. Fomalont et al. (1991) used the VLA to find the areal density of sources brighter than 50 μJy at 5 GHz to be $\sim 6.4 \times 10^{-5}$ arcsec^{-2}, making the probability of a chance positional coincidence $\sim 2 \times 10^{-3}$ (taking our search area to be the synthesized beam size). We therefore identify this source with LHS 2397a AB. The multi-frequency cleaning algorithm determines a spectral index of $\alpha = -0.4 \pm 0.2$ ($S_\nu \propto \nu^\alpha$). We imaged the source in the Stokes V parameter and made no detection, with an image rms of 5.4 μJy bm^{-1}. Taking the Stokes V upper limit to be three times this value, we find that $|V|/I \lesssim 25\%$. We searched for flares and other forms of variability using a visibility-domain analysis of the Stokes I data as described in Williams et al. (2013). No significant indications of variability were seen.

There is a 50 μJy (7σ) radio source in the image of the LHS 3406 field at RA = 18:43:20.72, Dec = +40:40:33.01, which is 15″ distant from the astrometric prediction. We checked the image astrometry against two NVSS sources (NVSS J184331+404756 and NVSS J184314+403302), finding agreement down to the ∼1.5″ uncertainty in the survey's astrometry. We conclude that this source is not LHS 3406. There are no sources within ∼1′ of our astrometric predictions in all of the other fields. In each of these cases, we place an

upper limit on the target flux density of three times the image rms. The field of LHS 523 was visited twice; no source is detected in the individual visits or in a deep image formed by combining the two datasets. The results of our radio observations, including flux densities, are summarized in Table 5. Derived parameters, including radio spectral luminosities, are presented in Table 8.

5. TRENDS IN RADIO AND X-RAY EMISSION

We have combined our new measurements with data from the literature to compile a comprehensive database of UCDs with both radio and X-ray observations. In Table 6, we list these objects and provide some of their properties. Different authors report X-ray luminosities that are integrated over varying energy regimes; for consistency we normalize all X-ray fluxes and luminosities to a common band of 0.2–2.0 keV. We used PIMMS to compute the appropriate conversion factors, evaluating flux ratios in a range of different plasma temperatures in the APEC model. The resulting factors are listed in Table 7. The conversion factors represent an approximate median for several temperatures in the range $kT = 0.4$–1.0 keV and are stable to within 5% for temperatures within this range. In Table 8 we report all paired UCD radio and X-ray luminosities available, giving detailed references and using simultaneous measurements when available.

Although we focused on X-ray and radio fluxes when constructing our database, it contains many ancillary measurements such as distances, spectral types, photometry, and effective temperatures. It is compiled from simple textual tables that are maintained in the Git distributed version control system, taking inspiration from the architecture of the Open Exoplanet Catalogue (Rein 2012). Its design is intended to enable continuous refinement in a decentralized, collaborative manner. Further details will be presented in a future publication.

5.1. *X-Ray Luminosity vs. Spectral Type*

Low-mass stars of spectral types earlier than M6 obey an X-ray activity/rotation relationship with "saturation" at $[L_{\rm X}/L_{\rm bol}] \sim -3$ (Pizzolato et al. 2003; Wright et al. 2011). Because main-sequence late-type stars are generally rapid rotators (Irwin & Bouvier 2008), most of them have X-ray emission around this saturation level, as demonstrated in Figure 5. The <M6 objects in this figure having $[L_{\rm X}/L_{\rm bol}] \gtrsim -2$ are likely flares. All come from the work of Riaz et al. (2006), who obtained 1080 M dwarf X-ray fluxes from the ROSAT All-Sky Survey, a fraction of which will inevitably have been measured during a flare. All of the <M6 objects with $[L_{\rm X}/L_{\rm bol}] \lesssim -4.5$ and measured $v \sin i$ are slow rotators, and thus their low levels of X-ray emission are expected. There is a noticeable underdensity of sources with $[L_{\rm X}/L_{\rm bol}] \sim -4$ or $[L_{\rm X}] \sim 28$; it can also be seen clearly in the data of Pizzolato et al. (2003). This underdensity is reminiscent of the "Vaughan-Preston gap" (Vaughan & Preston 1980), a similar feature seen in the distribution of various chromospheric activity indicators observed in F and G stars, for which a variety of explanations have been offered, including changes in dynamo modes, evolutionary stages of rapid angular momentum loss, or two distinct waves of star formation in the solar neighborhood (e.g., Durney et al. 1981). Somewhat surprisingly, we are unable to

Table 5
Results of VLA Analysis

Name	Integ. Time	S_ν	rms	Synthesized Beam		
				Major	Minor	PA
	(s)	(μJy)	(μJy bm^{-1})	(arcsec)	(arcsec)	(deg)
(1)	(2)	(3)	(4)	(5)	(6)	(7)
LHS 292	2260	<23	7.7	5.0	2.7	−32
LHS 523	4405	<13	4.4	4.2	2.5	41
LHS 2397a AB	2335	63 ± 7	5.3	4.2	2.8	1
LHS 3406	2205	<16	5.4	3.5	3.0	108
LP 647−13	2265	<22	7.4	4.5	2.9	33
LP 851−346	2205	<19	6.2	7.1	2.8	−29
NLTT 40026	2205	<16	5.3	3.1	2.7	−43

Note. — Col. (4) is the background rms in a region near the source. Cols. (5) and (6) are FWHM sizes. The reference frequency of each image is 6.05 GHz. Further parameters regarding the detection of LHS 2397a AB are given in the text.

Table 6
UCDs with Both Radio and X-ray Measurements

2MASS Identifier	Other Name	SpT	J (mag)	K (mag)	d (pc)	$[L_{\rm bol}]$ $[L_\odot]$	References	
							(S)	(D)
(1)	(2)	(3)	(4)	(5)	(6)	(7)	(S)	(D)
¶ 10481258−1120082	LHS 292	M6.5	8.86	7.93	4.5	−3.15	1	2
¶ 22285440−1325178	GJ 4281	M6.5	10.77	9.84	11.3	−3.13	3	2
13142039+1320011 AB	NLTT 33370 AB	M7	9.75	8.79	16.4	−2.40	4	4
14563831−2809473	LHS 3003	M7	9.96	8.93	6.4	−3.29	5	2
16553529−0823401	vB 8	M7	9.78	8.82	6.5	−3.21	1	6
¶ 11554286−2224586	LP 851−346	M7.5	10.93	9.88	9.7	−3.32	7	7
¶ 15210103+5053230	NLTT 40026	M7.5	12.01	10.92	16.0	−3.30	5	5
¶ 00275592+2219328 AB	LP 349−25 AB	M8	10.61	9.57	13.2	−2.93	5	8
03205965+1854233	LP 412−31	M8	11.76	10.64	14.5	−3.29	5	9
¶ 11214924−1313084 AB	LHS 2397a AB	M8	11.93	10.73	14.3	−3.36	10	2
¶ 18432213+4040209	LHS 3406	M8	11.31	10.31	14.1	−3.16	5	2
19165762+0509021	vB 10	M8	9.91	8.77	6.1	−3.30	11	11
14542923+1606039 Bab	Gl 569 Bab	M8.5	10.61	9.45	9.8	−3.17	12	13
18353790+3259545	LSPM J1835+3259	M8.5	10.27	9.17	5.7	−3.52	5	9
¶ 01095117−0343264	LP 647−13	M9	11.69	10.43	11.1	−3.48	5	5
03393521−3525440	LP 944−20	M9	10.72	9.55	5.0	−3.81	5	9
08533619−0329321	LHS 2065	M9	11.21	9.94	8.5	−3.52	5	2
10481463−3956062		M9	9.54	8.45	4.0	−3.54	14	15
14284323+3310391	LHS 2924	M9	11.99	10.74	10.8	−3.63	15	2
15010818+2250020	TVLM 513−46546	M9	11.87	10.71	9.9	−3.67	15	2
00242463−0158201	BRI B0021−0214	M9.5	11.99	10.54	12.1	−3.49	16	2
00274197+0503417	PC 0025+0447	M9.5	16.19	14.96	72.0	−3.67	17	17
07464256+2000321 AB		L0	11.76	10.47	12.2	−3.36	18	5
06023045+3910592	LSR J0602+3910	L1	12.30	10.87	10.6	−3.67	19	19
13054019−2541059 AB	Kelu−1 AB	L2	13.41	11.75	18.7	−3.56	5	5
05233822−1403022		L2.5	13.08	11.64	13.4	−3.82	5	9
00361617+1821104	LSPM J0036+1821	L3.5	12.47	11.06	8.8	−3.99	20	15
12281523−1547342 AB		L5	14.38	12.77	20.3	−3.93	5	5
15074769−1627386		L5	12.83	11.31	7.3	−4.23	20	9

References. — Columns are (S), spectral type; and (D), distance. [1] Henry et al. (1994), [2] van Altena et al. (1995), [3] Kirkpatrick et al. (1991), [4] Lépine et al. (2009), [5] Cruz et al. (2003), [6] Gliese & Jahreiß (1991), [7] Crifo et al. (2005), [8] Gatewood & Coban (2009), [9] Cruz et al. (2007), [10] Freed et al. (2003), [11] Berger et al. (2008b), [12] Zapatero Osorio et al. (2004), [13] Stelzer (2004), [14] Reiners & Basri (2010), [15] Reid et al. (2008), [16] Reid et al. (1995), [17] McLean et al. (2012), [18] Berger et al. (2009), [19] Berger et al. (2010), [20] Berger et al. (2005)

Note. — Rows marked with a pilcrow (¶) indicate sources with new measurements presented in this work. Col. (3) is spectral type. Cols. (4) and (5) are from 2MASS (Skrutskie et al. 2006). Col. (7) is the bolometric luminosity, the calculation of which is described in the Appendix; note that here it is given in units of $L_\odot$, not cgs.
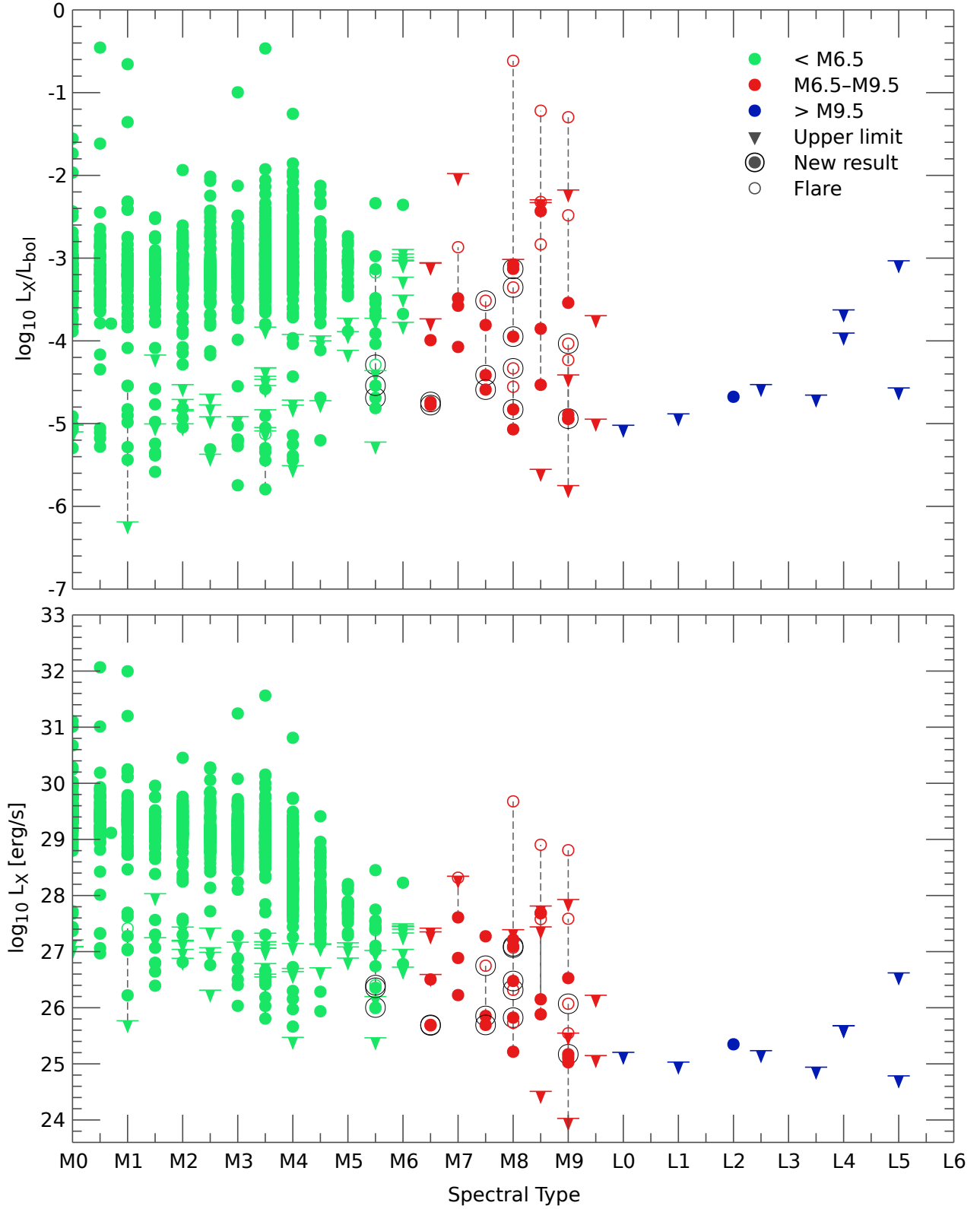
Figure 5. X-ray luminosity as a function of spectral type, both normalized by L_{bol} (*upper panel*) and unnormalized (*lower panel*). L_X is in the 0.2–2 keV band. Objects with adopted spectral types of M6 or earlier, M6.5–M9.5, and L0 or later are plotted in *green*, *red*, and *blue*, respectively. Upper limits are represented by *downward-pointing triangles*. *Dashed lines* connect multiple measurements of the same source, with *open symbols* denoting known flaring emission. Measurements from this work are highlighted with *black circles*. Both the normalized and unnormalized luminosities appear to have a typical scale in earlier-type objects (10^{-3} and $10^{29.3}$ erg s^{-1}, respectively) with a falloff in later-type objects, although the starting point for the falloff differs between the two cases ($\sim$M5 and $\sim$M3.5, respectively) due to the evolution of L_{bol} with spectral type.

Table 7
X-Ray Band
Conversion
Factors

Band (keV)	Factor
0.1–2.4	0.84
0.1–10.0	0.80
0.2–8.0	0.95
0.3–0.8	1.53
0.3–2.0	1.10
0.3–7.0	1.05
0.3–8.0	1.05
0.3–10.0	1.05
0.5–8.0	1.20

locate in the literature any investigation of this feature; such an undertaking is beyond the scope of this work.

Figure 5 shows that our observations lend further support to the conclusion that the standard X-ray "saturation" effect breaks down at spectral types $\gtrsim$M6 (Fleming et al. 2003; Berger et al. 2010), an effect that is also seen in $L_{\mathrm{H}\alpha}/L_{\mathrm{bol}}$ (Gizis et al. 2000; Mohanty & Basri 2003). Although the cause of this breakdown has been the subject of much study, the number of detected objects is small while there are many possibly-relevant physical effects: decreasing T_{eff}, increasing rotation, a disappearing radiative core, and an increasingly dipolar magnetic field (Morin et al. 2008). The role of rotation is of particular interest because of its known effect on X-ray activity and its strong correlation with spectral type; this issue is explored in Paper II.

The data show a similar breakdown in terms of L_{X}, with $[L_{\mathrm{X}}] \approx 29.3$ for spectral types $\lesssim$M4 but decreasing by a factor of $\sim$10 for each later spectral subtype. This empirical relationship indicates a breakdown of the relationship around where full convection sets in, at spectral types of $\gtrsim$M3.5–M4 (Chabrier & Baraffe 2000). Furthermore, there are indications that it may be more appropriate to consider L_{X} rather than $L_{\mathrm{X}}/L_{\mathrm{bol}}$ in this regime: results from Zeeman-Doppler imaging studies suggest that mid-to-late M dwarfs harbor relatively weak, disordered magnetic fields similar to those of slowly-rotating solar-type stars (Morin et al. 2010), and there is substantially less scatter in the slow-rotator region of the X-ray activity/rotation relationship when L_{X} rather then $L_{\mathrm{X}}/L_{\mathrm{bol}}$ is considered (Pizzolato et al. 2003).

5.2. *The Güdel-Benz Relation*

Our paired radio and X-ray observations allow us to consider ultracool dwarfs in the context of the GBR. This is particularly salient in the UCD regime because the first detection of radio emission from a brown dwarf implied a severe divergence from the GBR (Berger et al. 2001), and subsequent observations have confirmed that this divergence is not uncommon (e.g., Berger et al. 2008a, 2010). In Figure 6, we plot our full database of UCDs with both radio and X-ray measurements as well as the original data of Benz & Güdel (1994). Figure 7 is similar but omits known flares. In these and several subsequent plots, we show the best linear fit to the Benz & Güdel (1994) data from Berger et al. (2010),

$$[L_{\nu,\mathrm{R}}] = 1.36([L_{\mathrm{X}}] - 18.97). \qquad (2)$$

The scatter of the Benz & Güdel (1994) data around this fit is 0.6 dex when L_{X} is treated as an independent variable (i.e., the distance from the best-fit line is measured at fixed L_{X}). The scatter relative to the best-fit line (i.e., measured perpendicular to it) is 0.2 dex. In the Benz & Güdel (1994) dMe data, $[L_{\nu,\mathrm{R}}/L_{\mathrm{X}}] \sim -15.5$ typically, a value we adopt as a reference when quantifying radio over-luminosity relative to the GBR.

As may be seen in Figure 6, almost all of our new results could be consistent with the established GBR. Since the radio upper limits are $\sim$2 dex above the best-fit line. The lone new radio detection, LHS 2397a AB, has $[L_{\nu,\mathrm{R}}/L_{\mathrm{X}}] = -13.9$ and lies 1.3 dex away from the best-fit line. It is thus an outlier but not nearly as extreme as, for example, TVLM 513–46546, which has $[L_{\nu,\mathrm{R}}/L_{\mathrm{X}}] = -11.5$ and is 3.2 dex away from the fit in quiescence. We find no significant signs of variability in the emission of LHS 2397a AB in either band, which suggests that the observed fluxes correspond to a quiescent rather than flaring state. LP 349–25 AB, for which we have combined a new X-ray analysis with a radio measurement from the literature, has $[L_{\nu,\mathrm{R}}/L_{\mathrm{X}}] = -12.0$ and lies 2.7 dex away from the best-fit line in quiescence, making it a strong violator of the GBR.

UCD emission in both the radio and X-ray bands can show significant flaring during typical observational timescales (e.g., Berger et al. 2001; Burgasser & Putman 2005; Rutledge et al. 2000; Stelzer et al. 2006b), and the radio emission is additionally known to evolve over $\sim$year timescales in some cases (e.g., Antonova et al. 2007). The simultaneity of measurements is thus important to consider in the context of the GBR. In Table 8, we annotate which radio/X-ray measurements arise from simultaneous observations, and we isolate these measurements in Figure 8. Simultaneous observations constitute about one third of the existing dataset, with many of the measurements coming from an observational campaign we have conducted over the past several years (Berger et al. 2005, 2008b,a, 2009, 2010, Williams et al., in preparation). These simultaneous measurements include several of the most extreme GBR violators, showing that strong divergence from the GBR is a genuine phenomenon and *not* merely due to flaring. There is only one simultaneously-observed UCD to be detected in the X-ray but not the radio: the L2+L3.5 ($\pm$1 subtype) binary Kelu-1 AB (Audard et al. 2007). Its detection by *Chandra* was marginal (4 counts), precluding a detailed analysis.

In Figure 9 we plot $L_{\nu,\mathrm{R}}/L_{\mathrm{X}}$ as a function of spectral type. *There is clear evidence for new behavior at spectral types $\geq$M7*: while there are no measurements of $[L_{\nu,\mathrm{R}}/L_{\mathrm{X}}] > -13$ in objects earlier than M7, there are seven in later objects. The lower panel plots distance from the GBR linear fit (Equation 2) rather than the simple ratio $L_{\nu,\mathrm{R}}/L_{\mathrm{X}}$. As can be seen, the choice of ordinate does not significantly affect the structure of the data, and we discuss trends in terms of $L_{\nu,\mathrm{R}}/L_{\mathrm{X}}$ because that quantity is closer to the observables.

In both panels of Figure 9, divergence from the GBR seems to increase unconditionally with spectral type. This seeming trend is partially misleading because of radio sensitivity limitations. While there is new behavior at spectral types $\geq$M7, a population of $\geq$M7 objects consistent with the early- and mid-M dwarfs ($[L_{\nu,\mathrm{R}}/L_{\mathrm{X}}] \sim -15.5$) is not excluded. The new observations presented in this
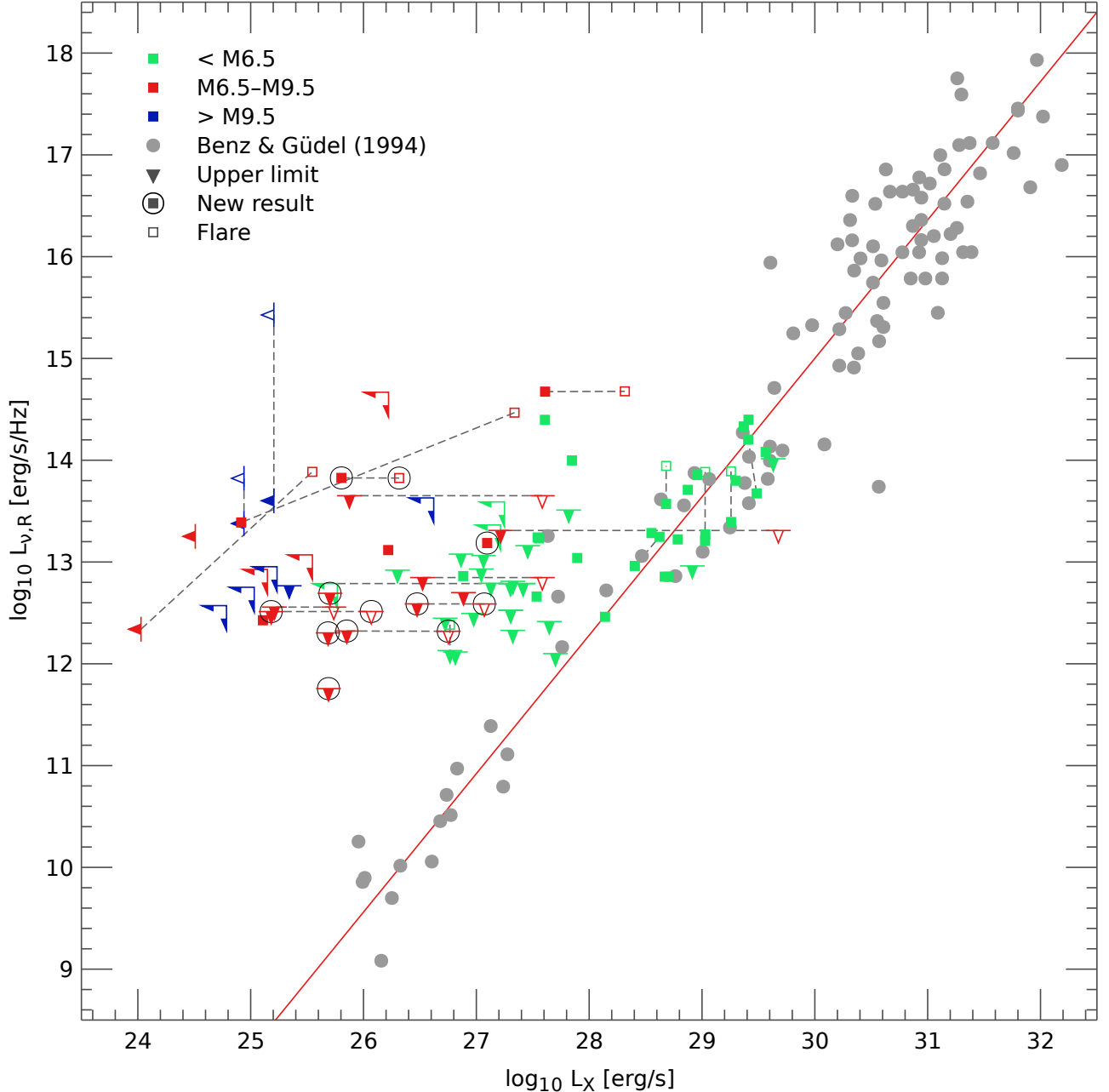
Figure 6. The "Güdel-Benz" relationship (GBR) between L_X (0.2–2 keV) and $L_{\nu,R}$. Colors and symbols are as in Figure 5, with limits shown by triangles pointing down, left, or down-left. Data for objects M6.5 or later (*red* and *blue* symbols) are tabulated in Table 8. *Gray circles* reproduce the original data of Benz & Güdel (1994): those with $[L_{\nu,R}] < 12$ are solar flares; $12 < [L_{\nu,R}] \lesssim 14.5$ are dMe and dKe stars; $[L_{\nu,R}] \gtrsim 14.5$ are active binaries. Except for LP 349–25 AB, the new data do not show the extreme radio over-luminosity of some previous observations, being consistent with radio over-luminosities of $\lesssim 10^2$ compared to the GBR.

work, which are of nearby objects and were obtained with a highly sensitive radio telescope (the upgraded VLA), reach limits of $[L_R] \sim 12.5$. As shown in Figure 6, our data include the most sensitive upper limit on M dwarf radio emission available, $[L_{\nu,R}] < 11.8$ for LHS 292. Nonetheless, in our sample $[L_X] \sim 26$, so that we are insensitive to $[L_{\nu,R}/L_X] \lesssim -13.5$. A source obeying the GBR with $[L_X] = 26$ and $d = 10$ pc would have a radio flux density of $S_\nu \sim 30$ nJy, accessible only to the proposed Square Kilometer Array (SKA; Carilli & Rawlings 2004). Until the arrival of an SKA-class telescope, the only way to probe UCDs in this regime will

be through observations of objects at distances of $\lesssim 3$ pc, such as the recently-discovered L/T binary Luhman 16 (Luhman 2013; Burgasser et al. 2013).

Another issue affecting Figure 9 is the correlation between mass and rotational velocity in main-sequence late-type stars (e.g., Irwin & Bouvier 2008), which obscures the true physical process underlying the observed trend. We plot $L_{\nu,R}/L_X$ as a function of $v \sin i$ in Figure 10. Similar to Figure 9, $L_{\nu,R}/L_X$ appears to increase with $v \sin i$ but the trend requires care in interpretation. Along with the limitations in sensitivity to small values of $L_{\nu,R}/L_X$, some objects with low values of $v \sin i$ may be rapid rota-
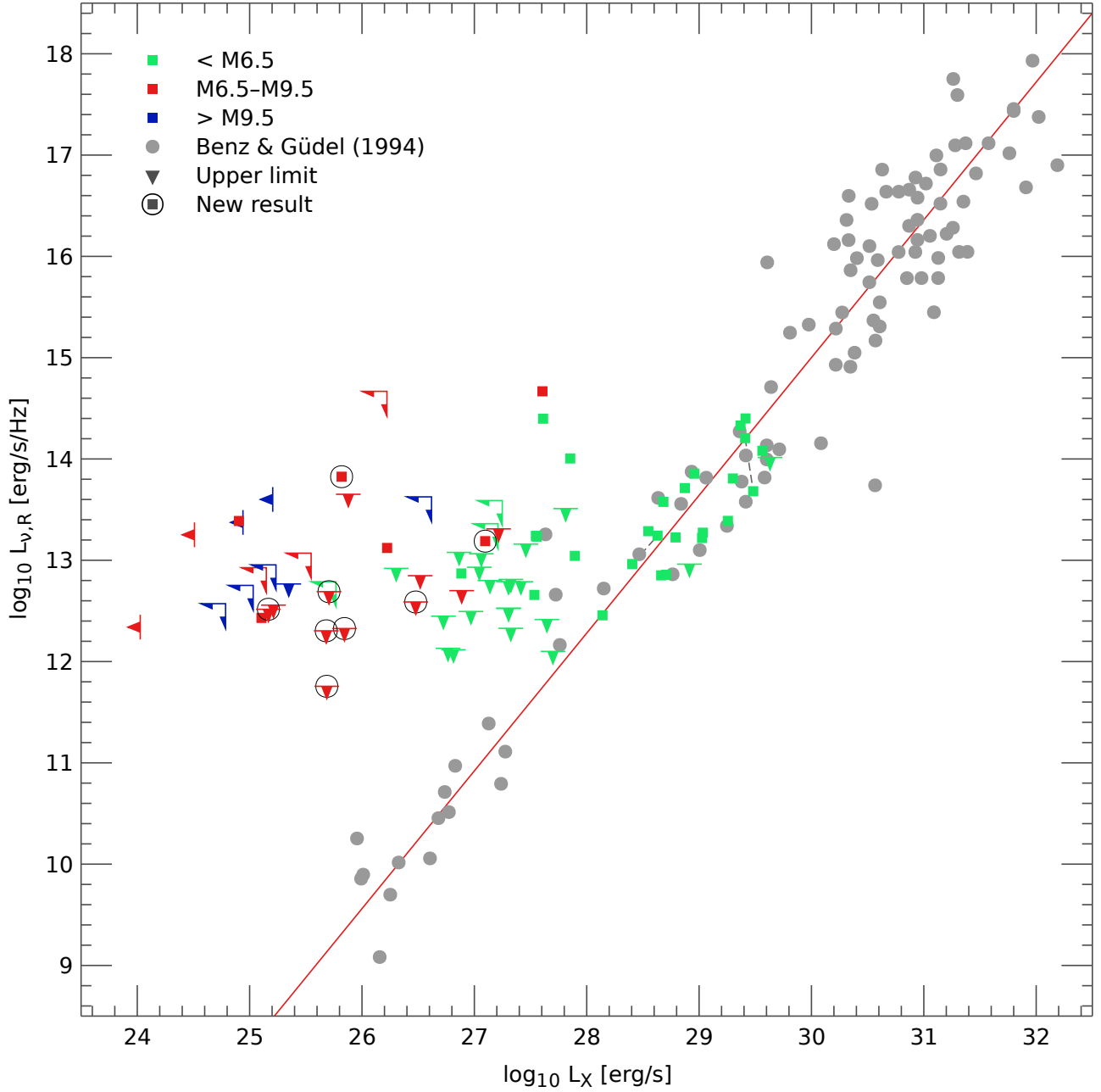
Figure 7. The same as Figure 6, but omitting known flares.

tors seen at low inclinations. In this context, it is striking that out of 13 objects with $v \sin i > 20$ km s^{-1}, seven have $[L_{\nu,R}/L_X] > -13.5$; that is, the fraction of radio-over-luminous objects is large. The lack of radio-over-luminous sources with small values of $v \sin i$ is consistent with the argument of Hallinan et al. (2008) that viewing angle is an important factor affecting the observed radio emission: if $L_{\nu,R}/L_X$ increases with v but is independent of $\sin i$, there should exist sources seen nearly pole-on with low values of $v \sin i$ and large radio excess. Such sources have not yet been observed. The presence of both lower and upper limits at high values of $v \sin i$ prevents a simple characterization of the trend in $L_{\nu,R}/L_X$. A more full analysis should not only account for inclination effects, but also for source-to-source variation. Studies of the relationship between X-ray emission and rotation

have shown that a useful parameter for doing so is the Rossby number, $Ro = P_{rot}/\tau_{conv}$, where P_{rot} is the rotation period and τ_{conv} is the characteristic convective overturn time (Noyes et al. 1984; Pizzolato et al. 2003). We pursue these matters in Paper II.

Finally, although we have discussed departure from the GBR in terms of "radio over-luminosity," it could clearly be expressed in terms of "X-ray under-luminosity" as well, a framing well-motivated by the dropoff in L_X/L_{bol} seen in UCDs. This prompts us to consider a modification of the GBR in terms of the benchmark "saturation" level of X-ray emission, defining $L_{X,sat} = 10^{-3} L_{bol}$. In Figure 11 we plot the same radio data as in Figure 6 but replace L_X with $L_{X,sat}$. We omit flaring measurements and do not alter the data from Benz & Güdel (1994). As should be expected from Figure 5, the UCD mea-
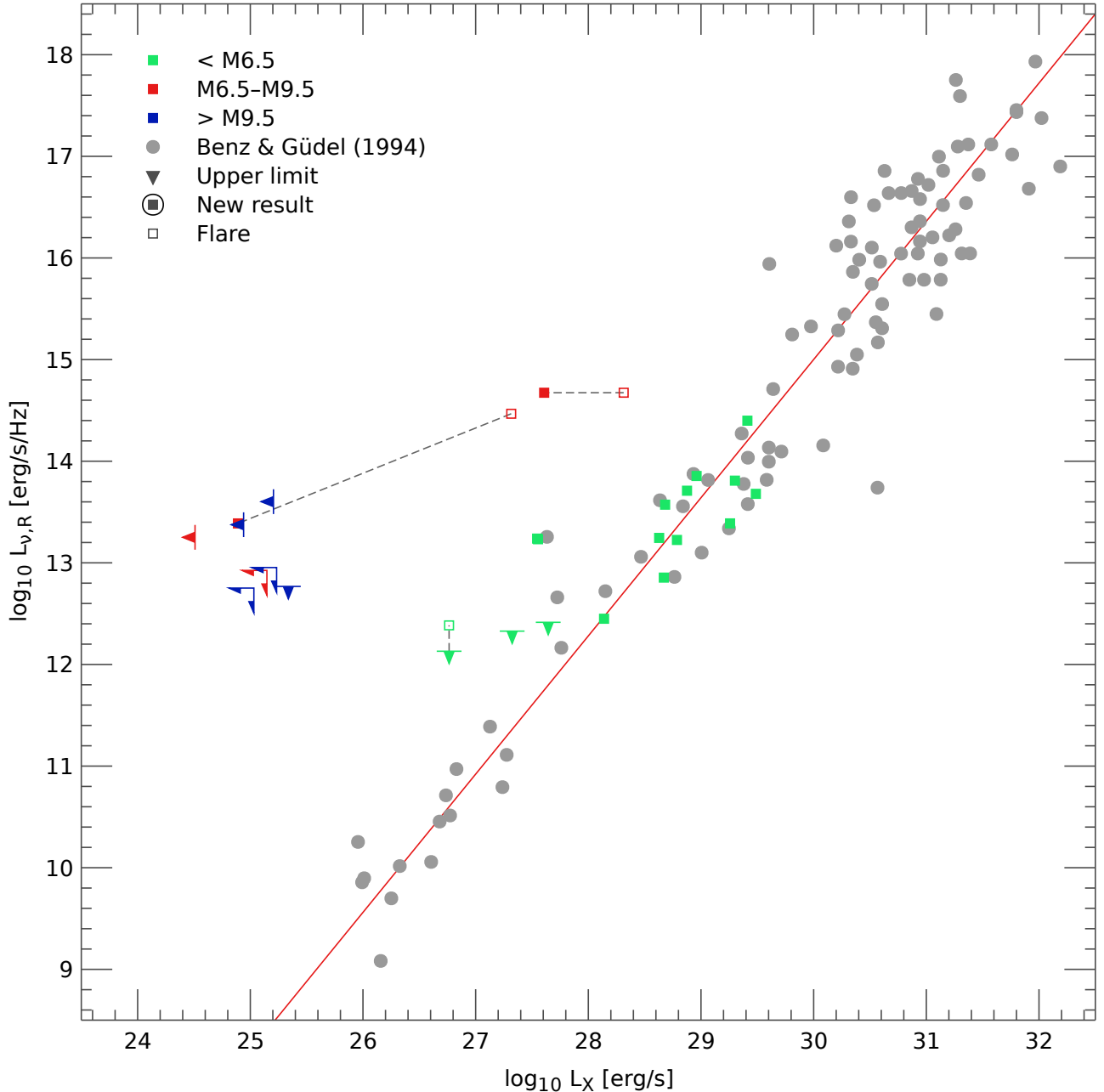
Figure 8. The same as Figure 5, but including only UCDs with simultaneous radio and X-ray observations. Some of the most extreme instances of UCD radio over-luminosity come from simultaneous observations, firmly establishing that variability is not responsible for the observed behavior. Objects earlier than M6.5 with simultaneous observations are consistent with the GBR, while those with non-simultaneous observations present a more ambiguous picture (cf. Fig 6).

surements move closer to the canonical GBR. The data for objects $<$M6.5 straddle the canonical relation nicely, with a substantial subset of measurements that are radio *under*luminous. The UCDs, however, remain displaced to the left of the GBR; in other words, even if they emitted X-rays at the canonical "saturation" level, they would still be over-luminous in the radio. Any explanation of GBR divergence in UCDs must therefore not merely account for the suppression of X-ray emission relative to the stellar "saturation" trends, but also account for a comparative increase in radio emission. For instance, if the suppression of UCD X-ray emission is entirely due to less efficient heating of the corona leading to a temperature apprecia-

bly lower than the typical coronal value of $\approx$1 keV (e.g., Berger et al. 2008a), a mechanism must still be proposed to explain the unexpectedly bright radio emission. We argue below that in the radio-over-luminous sources, $L_{\nu,\mathrm{R}}$ no longer scales with L_{bol}.

5.3. *Summary of Observed Trends*

The X-ray emission of UCDs drops off rapidly with spectral type, with slightly different properties depending on whether L_{X} or $L_{\mathrm{X}}/L_{\mathrm{bol}}$ is considered (Figure 5). Some UCDs diverge strongly from the GBR, with values of $L_{\nu,\mathrm{R}}/L_{\mathrm{X}}$ exceeding the typical value of $10^{-15.5}$ by 4 orders of magnitude; others may be consistent with it, with
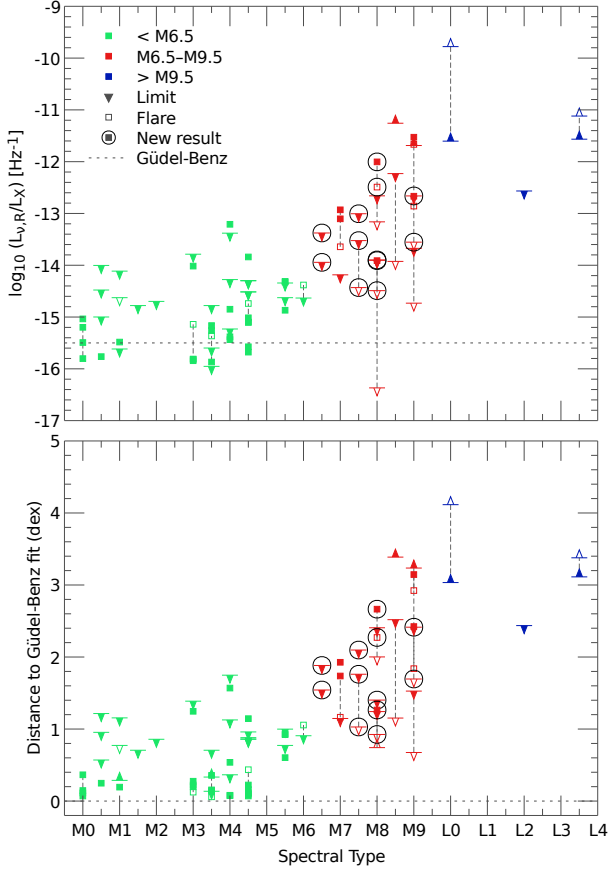
Figure 9. *Upper panel:* measured ratios of radio to X-ray luminosities as a function of spectral type. Colors and symbols are as in Figure 5. The first measurement in which $[L_{\nu,\mathrm{R}}/L_\mathrm{X}] > -13$ is at spectral type M7. The reference line of $[L_{\nu,\mathrm{R}}/L_\mathrm{X}] = -15.5$ is appropriate for the GBR at SpT $\sim$ M0–M6 (Berger et al. 2010). *Lower panel:* same underlying data as the upper panel, but now plotting distance from the linear fit to the Güdel-Benz relationship (Equation 2) rather than $L_{\nu,\mathrm{R}}/L_\mathrm{X}$. The overall structure is virtually identical.
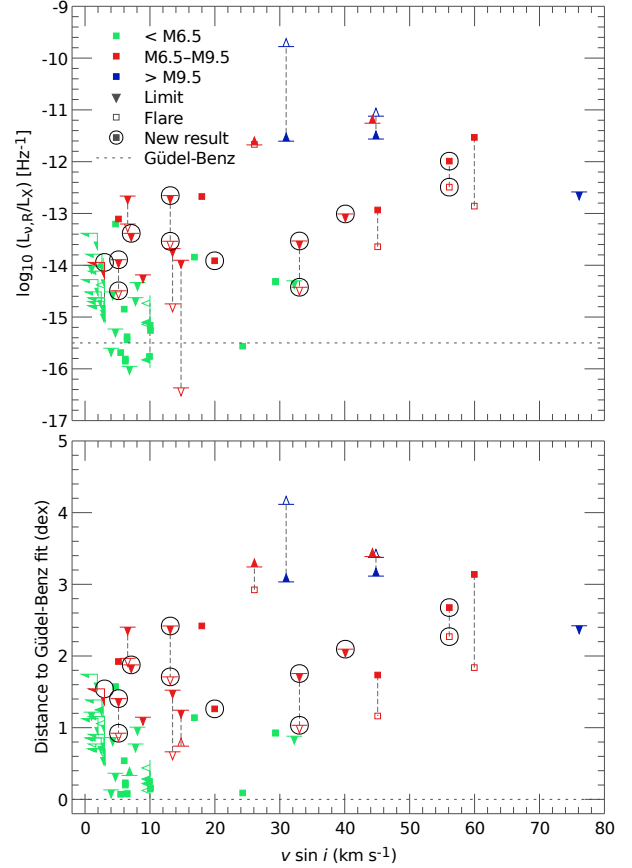
Figure 10. *Upper panel*: measured ratios of radio to X-ray luminosities as a function of projected rotational velocity, $v \sin i$. Colors and symbols are as in Figure 5. *Lower panel:* same underlying data as the upper panel, but now plotting distance from the linear fit to the Güdel-Benz relationship (Equation 2) rather than $L_{\nu,\mathrm{R}}/L_\mathrm{X}$.

the limited sensitivity of radio observations allowing us only to conclude that $[L_{\nu,\mathrm{R}}/L_\mathrm{X}] \lesssim -13.5$ (Figure 6). Although variability is an important consideration, extreme GBR divergence is seen in simultaneous radio and X-ray observations, confirming its reality (Figure 8). More extreme divergence from the GBR seems to become possible at later spectral types (Figure 9). Even if UCD X-ray activity ($L_\mathrm{X}/L_\mathrm{bol}$) did not drop off rapidly with spectral type, but rather remained at the standard "saturation" level of $[L_\mathrm{X}/L_\mathrm{bol}] = -3$, UCDs would still be radio-over-luminous compared to the GBR (Figure 11).

The interpretation of these trends is complicated by the correlation between mass and rotational velocity in main-sequence late-type stars (e.g., Irwin & Bouvier 2008). Only objects with $v \sin i \gtrsim 20$ km s^{-1} are seen to diverge strongly from the GBR, and $\approx$50% of such objects do so (Figure 10). Although we discuss the role of rotation below, we defer detailed investigation of the relationship between rotation and magnetic activity in UCDs to Paper II.

6. DISCUSSION

Our results underscore the wide range of magnetic phenomenology seen in the UCD regime. For instance, our

new observations of the M7.5 dwarf LP 851–346 yield a radio over-luminosity of $\lesssim$2.5 orders of magnitude. Meanwhile, simultaneous observations of the nearby M8.5 dwarf LSR J1835+3259 have revealed a radio over-luminosity of $\gtrsim$5 orders of magnitude (Berger et al. 2008b; Hallinan et al. 2008); this assessment is relative to its mean radio emission ($\sim$0.5 mJy), not the bright, highly polarized pulses that it has also been seen to emit ($\sim$2 mJy; Hallinan et al. 2008). Both objects are relatively rapid rotators, with $v \sin i = 33$ and 50 km s^{-1}, respectively. (We emphasize that while inclination effects may cause a rapid rotator to appear as a slow rotator, they cannot cause a slow rotator to appear as a rapid rotator.) Both are nearby (9.7 and 5.7 pc; Crifo et al. 2005; Reid et al. 2003), and neither is known to have a companion (e.g., Faherty et al. 2009; Siegler et al. 2005). Despite these similarities, our new data show that while LP 851–346 is least an order of magnitude brighter than LSR J1835+3259 in the X-ray, it is also at least an order of magnitude fainter in the radio.

Stelzer et al. (2012) considered the GBR in the UCD regime and proposed the existence of two populations: one comprising rapidly rotating, radio-bright, X-ray-dim UCDs; the other comprising slower-rotating, radio-dim, X-ray-bright objects. They additionally noted that only the radio-bright objects display bright, highly polarized radio pulses, while only the radio-dim objects produce
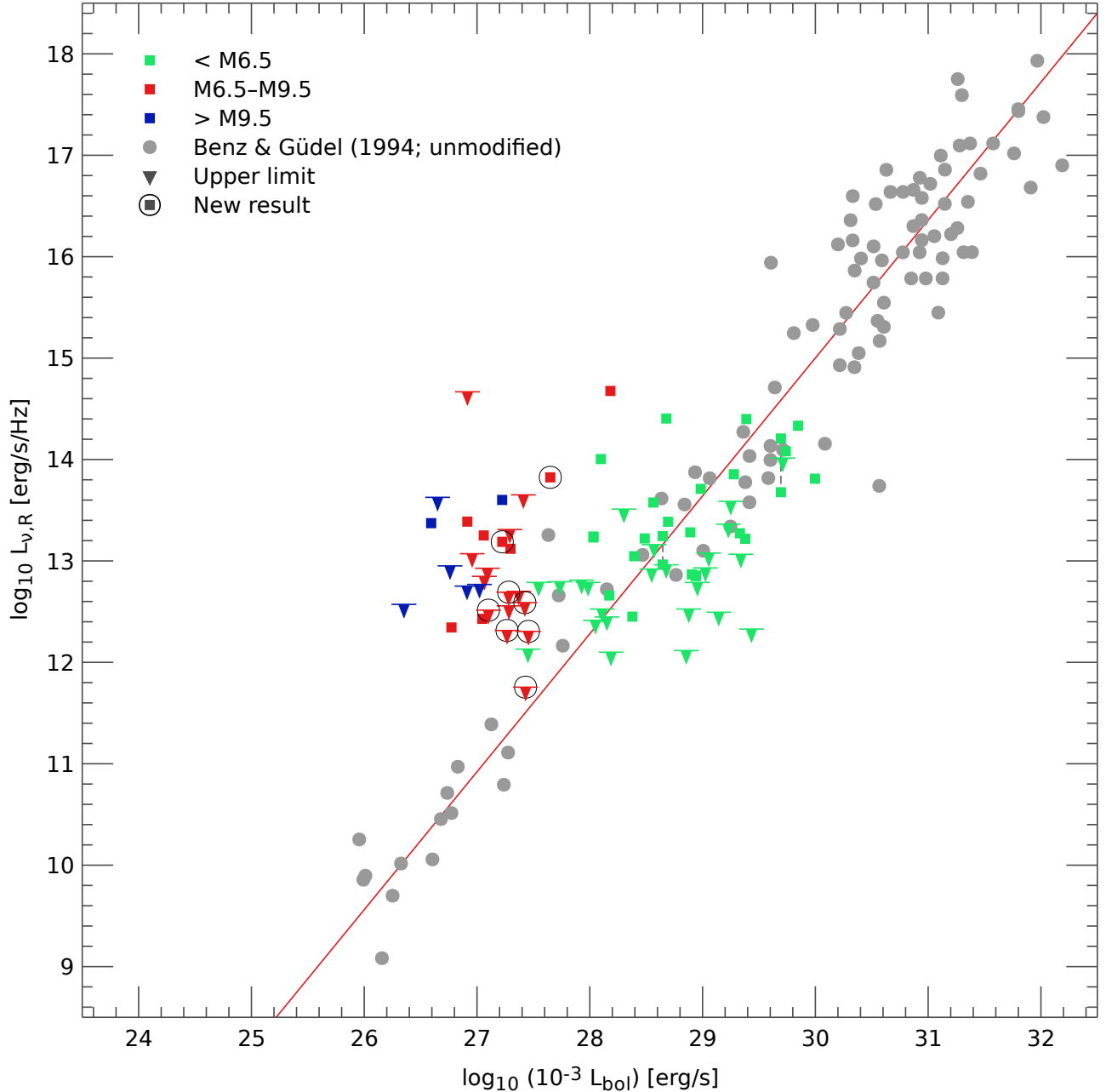
Figure 11. A "pseudo Güdel-Benz" relationship between $L_{\nu,R}$ and the hypothetical "saturated" X-ray luminosity associated with each star, $L_{X,sat} = 10^{-3}L_{bol}$. Colors and symbols are as in Figure 5. The data from Benz & Güdel (1994) (*gray circles*) have not been modified. Even if UCDs (*blue and red points*) emitted X-rays at typical dMe "saturation" levels, they would still be radio-over-luminous compared to the GBR. If <M6.5 dwarfs emitted X-rays at these levels, on the other hand, they would cluster around the GBR.

X-ray flares, with the exception of LP 944–20 which seems to flare in both bands. Our data show that rotational velocity is not strictly tied to this dichotomy. LP 851–346 and NLTT 40026 are both rapid rotators (33 and 40 km s^{-1}, respectively) that are nonetheless radio dim and X-ray bright. The late-M binary NLTT 33370 AB is also a rapid rotator (45 km s^{-1}; McLean et al. 2011) that has relatively low divergence from the GBR, being radio over-luminous by ∼2.5 orders of magnitude in quiescence (Williams et al. 2013, in preparation).

We propose that the range of observed UCD behavior may be due to varying topology of their magnetic fields. In their study of the relationship between rotation and radio

activity in UCDs, McLean et al. (2012) proposed such a connection; here, we extend it to include X-ray emission as well. The connection to magnetic topology is motivated by a series of studies of M dwarfs using Zeeman-Doppler imaging (ZDI) techniques (Donati et al. 2008; Morin et al. 2008, 2010). In ZDI, the magnetic field topology is reconstructed from measurements of the Zeeman effect in time-resolved optical spectropolarimetry (Semel 1989)[4].

---

[4] While the Zeeman effect provides a direct measurement of the field, it is important to note that the quantity being measured is the net signed field in each resolution element. Comparisons with measurements of the total field from FeH spectroscopy indicate that ZDI is sensitive to ≲15% of the total field (Reiners & Basri 2009).

Morin et al. (2010) find that some M dwarfs have strong, axisymmetric fields, while others have fields that are weak and non-axisymmetric. While early-M dwarfs inhabit the weak-field regime and mid-M dwarfs inhabit the strong-field regime, late-M dwarfs inhabit *both* regimes. This observational finding led Morin et al. (2010) to propose two magnetic dynamo modes leading to differing magnetic topologies, with late-M dwarfs having a bistable dynamo that may inhabit either mode. This concept is supported by recent results from geodynamo simulations that show bimodal dynamo outcomes in rapid rotators (Morin et al. 2011; Gastine et al. 2013).

We suggest that UCDs with strong, axisymmetric fields tend to have values of $L_{\nu,\mathrm{R}}/L_\mathrm{X}$ in line with the GBR, while the ones with weak, non-axisymmetric fields are radio over-luminous. Slow rotators ($\lesssim$20 km s^{-1}) have strong-field dynamos and thus stay close the GBR, as found by Stelzer et al. (2012). Rapid rotators may have dynamos in either mode, so some are strong GBR violators while others are not, explaining the results of McLean et al. (2012) and this work. The association of sources that stay near the GBR with strong fields provides continuity with the ZDI and X-ray observational results for mid-M dwarfs. The similar patterns seen in the ZDI topology and $L_{\nu,\mathrm{R}}/L_\mathrm{X}$ results are the primary motivation for our hypothesis.
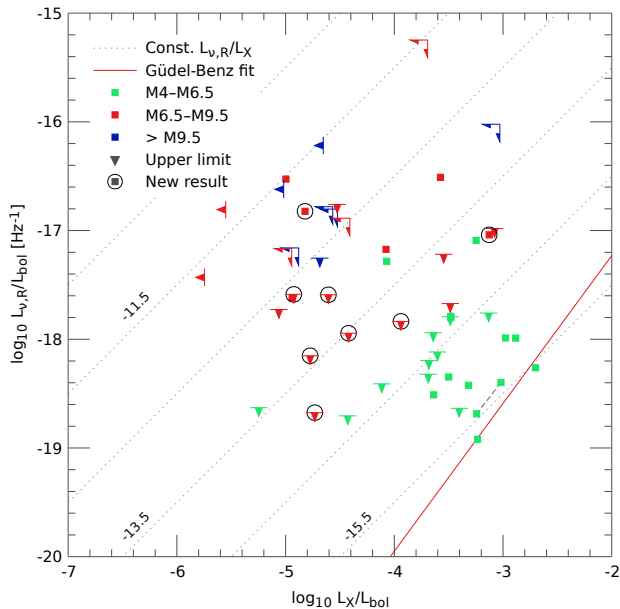

Figure 12. $L_{\nu,\mathrm{R}}/L_\mathrm{bol}$ against $L_\mathrm{X}/L_\mathrm{bol}$ in fully-convective cool dwarfs. Symbols are as in Figure 6, except that *green points* include only M4–M6.5 dwarfs. *Dotted diagonal lines* indicate constant values of $L_{\nu,\mathrm{R}}/L_\mathrm{X}$. *Red line* matches the slope of the fit to the Güdel-Benz relation in Figure 6 and passes through the point representing Gl 166 C (M4.5), which has simultaneous radio and X-ray observations and lies extremely close to the fit given in Equation 2.

We have described the difference between the proposed strong-field and weak-field sources in terms of $L_{\nu,\mathrm{R}}/L_\mathrm{X}$, and argued that the weak-field sources are radio over-luminous and X-ray under-luminous. However, the weak-field sources also tend to have later spectral types, and as shown in Figure 5 these sources have lower values of L_X. Some component of the X-ray under-luminosity of the

weak-field sources may be due to their cooler temperates rather than the proposed effects of field topology. To clarify this issue, we plot in Figure 12 a modified Güdel-Benz relation in which we restrict the data to fully-convective dwarfs and normalize by L_bol, thereby rearranging the data points along lines of constant $L_{\nu,\mathrm{R}}/L_\mathrm{X}$. It is noteworthy that even after accounting for changes in L_bol, the radio-bright sources are still X-ray underluminous compared to the radio-dim ones. Hypothetically, if the mean L_bol of the radio-bright objects were *much* lower than that of the radio-dim objects, the two groups might have indistinguishable values of $L_\mathrm{X}/L_\mathrm{bol}$, and the scatter in Figure 12 might be narrow in the $L_\mathrm{X}/L_\mathrm{bol}$ direction and broad in the $L_\mathrm{R}/L_\mathrm{bol}$ direction. This is not the case. Instead, even after taking the changing L_bol into account, the radio-bright sources seem to require both smaller $L_\mathrm{X}/L_\mathrm{bol}$ and larger $L_{\nu,\mathrm{R}}/L_\mathrm{bol}$. We argue below that for the radio-bright sources $L_{\nu,\mathrm{R}}$ is in fact a more appropriate quantity to consider than $L_{\nu,\mathrm{R}}/L_\mathrm{bol}$, whereas for the radio-faint ones the opposite is true.

The obvious issue to consider in the bimodal dynamo scenario is how the two field topologies lead to such different values of $L_{\nu,\mathrm{R}}/L_\mathrm{X}$. We start first with the weak-field, radio-bright mode. It is plausible that this mode extracts energy from stellar convective motions less efficiently than the strong-field mode, leading to a decrease in overall magnetic activity that manifests itself in decreased $L_\mathrm{X}/L_\mathrm{bol}$ compared to the strong-field objects. Meanwhile, Figure 6 shows that these objects tend to have similar values of $[L_{\nu,\mathrm{R}}] \approx 13.5$. We conjecture that in this mode, tangled magnetic field structures lead to persistent small-scale reconnection events that are sufficient to maintain a population of gyrosynchrotron-emitting electrons filling a coronal region a few stellar radii (R_*) in size. This model has already been suggested for the radio-bright sources (e.g., Berger et al. 2008b, 2009; McLean et al. 2011). Because the radio luminosity is energetically unimportant compared to L_X or L_bol, the radio-emitting population could be maintained even at very low levels of magnetic activity. The observed spectral luminosity $L_{\nu,\mathrm{R}} \propto \nu^2 T_b R^2$, where T_b is the brightness temperature and R is the characteristic size of the emitting region. In the UCD regime, $R_* \sim R_J$ with very weak dependence on mass. Supposing $R \sim R_*$, we find that in the radio-bright population $T_b \sim 10^{8.5-9.5}$ K. These results are consistent with values found in the dM1e binary YY Gem, for which $T_b = 1.1 \times 10^9$ K and $R \sim 2R_*$ were derived from VLBI observations (Alef et al. 1997). Taking T_b to be insensitive to mass, $[L_{\nu,\mathrm{R}}] \approx 13.5$ should be a characteristic value for radio-bright UCDs observed at 8.5 GHz. Hallinan et al. (2008) pointed out the relatively stable values of $L_{\nu,\mathrm{R}}$ across the M spectral type and argued for a different emission mechanism (see below). Our interpretation differs in that we argue that emission from early-M dwarfs is instead due to magnetic reconnection in the standard chromospheric heating picture, leading to consistency with the GBR. In this scenario, the similar values of $L_{\nu,\mathrm{R}}$ in the early-M dwarfs and the radio-bright UCDs are coincidental.

In the strong-field mode, we hypothesize that the coupling to internal stellar convective motions is stronger, resulting in comparatively higher levels of magnetic activity and $L_\mathrm{X}/L_\mathrm{bol}$. These are nonetheless lower than what is found in rapidly-rotating earlier-type stars, an effect

often attributed to the outer layers of UCD atmospheres becoming appreciably neutral, reducing their coupling to the coronal magnetic field and thus their ability to inject energy into it through surface convective motions (Mohanty et al. 2002). The standard chromospheric evaporation model still applies, leading to values of $L_{\nu,\mathrm{R}}/L_\mathrm{X}$ compatible with the GBR. However, these objects are apparently unable to sustain a corona-filling population of gyrosynchrotron-emitting particles, perhaps because reconnection events are simply too rare. The rarer reconnection events would be more energetic than those seen in the weak-field sources, perhaps explaining the observation of Stelzer et al. (2012) that the radio-quiet sources are seen to flare in the X-ray while the radio-loud ones are not. This may also explain the conjecture of Robrade et al. (2010) that some UCDs exhibit large X-ray flares and low-level X-ray variability but, unlike active early-M dwarfs, not a continuous spectrum of flare energies.

A striking characteristic of the radio-bright UCDs is that several of them emit periodic, bright, highly polarized radio pulses (Hallinan et al. 2006, 2008; Berger et al. 2008a, 2009). These are characteristic of the electron cyclotron maser instability (ECMI; Wu & Lee 1979; Treumann 2006), a coherent process that results in radio emission at the cyclotron frequency $\omega_c = eB/mc$. This process is responsible for auroral radio bursts in the magnetic solar system planets, which have many similarities to those observed in the UCDs (Zarka 1998). In particular, the periodic nature of the pulses is strongly suggestive of beamed emission tied to the stellar rotation. We suggest that, despite their generally tangled fields, the weak-field sources are able to maintain the large-scale converging magnetic structures needed to produce these auroral bursts. These structures need not dominate the observed field and hence are consistent with the overall finding of a weak, non-axisymmetric field. We have argued that the weak-field sources maintain a population of energetic electrons filling the coronal volume, providing a continual supply of particles capable of driving the bursts as well. The strong-field sources are likely also able to maintain the requisite converging fields but, lacking the corona-filling supply of particles, do not display the periodic bursts. As pointed out by Stelzer et al. (2012), however, the strong-field sources are slower rotators, and so the lack of observed bursts may be a selection effect because UCD radio observations are generally shorter in duration than the rotational period. Hallinan et al. (2008) identify another possible selection effect, providing evidence that the sources with ECMI bursts are observed at high inclinations.

Hallinan et al. (2006, 2008) further argue that the GBR violators are radio bright because the vast majority of their radio emission is due to the ECMI, including the non-burst emission that has generally been attributed to gyrosynchrotron processes (e.g., Berger 2002, 2006). They suggest that depolarization and steady particle acceleration could cause ECMI emission to have the low variability and polarization that are associated with the non-burst emission of these sources. While this argument may apply to some UCDs, we disfavor its application to *all* of them, because it calls for an implausible physical configuration in sources such as 2MASS J07464256+2000321. This L dwarf binary periodically emits rapid ($\sim$100 s)

pulses of $\sim$10 mJy and $\sim$100% circular polarization atop seemingly quiescent emission at $\sim$0.3 mJy with $\lesssim$15% circular polarization and a spectral index of $\alpha \sim -0.7$ ($S_\nu \propto \nu^\alpha$) (Berger et al. 2009). Any variation besides the pulses is at the $\lesssim$1 mJy level. If the quiescent emission also originates in the ECMI, two emitting regions of identical field strengths would be required, both with the physical conditions suitable for ECMI cascade, but producing vastly different observed emission. It seems simpler to posit that both ECMI and gyrosynchrotron emission occur in this case. In other sources such as 2MASS J00361617+1821104, both polarized and unpolarized emission of comparable flux densities and variability characteristics are observed, and the arguments of Hallinan et al. (2006, 2008) are more persuasive.

In our scenario it is still not entirely clear what factors determine the overall level of magnetic activity, i.e. $L_\mathrm{X}/L_\mathrm{bol}$. There are substantial correlations among $L_\mathrm{X}/L_\mathrm{bol}$, spectral type (Figure 5), GBR deviation (Figure 12), and rotational velocity (Paper II). In the quest to understand these interconnections, two particular issues call for investigation. The first is to what extent the observed UCD "supersaturation" effect, an anticorrelation between $L_\mathrm{X}/L_\mathrm{bol}$ and $v \sin i$ (Berger et al. 2010), is a causal relationship, relating perhaps to evolution in the nature of the dynamo. The second is the question of which processes drive the observed dropoff in $L_\mathrm{X}/L_\mathrm{bol}$ as a function of spectral type (Figure 5), relating perhaps to rotation, changes in internal structure, or increased photospheric neutrality (Mohanty et al. 2002). Because of the correlations among the variables in question, the role of rotation must be considered carefully in attempts to resolve these issues, and so we defer further analysis to Paper II.

Finally, we wish to emphasize that although we have discussed a model of two distinct dynamo modes, these modes are not necessarily mutually exclusive within a given source – it is plausible that one object could host multiple field-generating processes. With a sample of 29 sources and many non-detections, it would be premature to claim that there are two distinct subpopulations.

7. SUMMARY AND CONCLUSIONS

We presented new X-ray (*Chandra*) and radio (VLA) observations of seven ultracool dwarfs with spectral types between M6.5 and M9.5 and a wide range of $v \sin i$. We have detected all of them in the X-ray band, nearly doubling the number of UCDs with X-ray detections. Despite the increased sensitivity of the upgraded VLA, only one of the sources was detected in the radio. Our results are thus broadly consistent with the Güdel-Benz relationship between radio and X-ray emission in stellar flare phenomena, though they still admit radio over-luminosities of a factor of $\sim$10^2. This is in contrast to several spectacular recent results, in which some UCDs are seen to be radio-over-luminous by $\sim$5 orders of magnitude. Although UCDs are highly variable in both bands, making simultaneous observations important tools in the analysis of correlations such as the GBR, we have argued that the nonsimultaneity of our observations does not significantly affect their interpretation.

We have also assembled a comprehensive sample of UCDs with both radio and X-ray observations (Figure 6; Table 8), including all known measurements in which

the observations were simultaneous. With the addition of our new measurements, there is strong evidence that UCDs display a wide range of behavior with regards to the GBR: some are strongly radio over-luminous, while others could be consistent with it. This range can be, and has been, interpreted as a bimodality in the UCD population (McLean et al. 2012; Stelzer et al. 2012), which has support from both ZDI observations and geodynamo simulations (Morin et al. 2010; Gastine et al. 2013). We have argued that one group of sources can maintain a population of gyrosynchrotron-emitting particles in the corona, setting an effective floor on $L_{\nu,\mathrm{R}}$, while the other group is less active than earlier-type stars but emits following the standard chromospheric evaporation model. Interpretation of the data, however, is made difficult by the many variables at play: M_*, T_{eff}, $v \sin i$, age, metallicity, binarity, and long- and short-term variability. It is not clear that the population can be neatly divided into two distinct subgroups at this time.

Although the study of UCD magnetism continues to present many puzzles, we see several reasons to be optimistic for the future. Studies of progressively larger samples will help clarify trends and allow more robust examination of subsamples that control for variables such as mass, age, or rotation. The upgrade of the VLA presents a major opportunity in this regard, because it is becoming clear that radio observations present the best opportunity for exploring the magnetism of the coolest objects, whose faintness and rapid rotation make extremely difficult the application of techniques such as ZDI. Furthermore, new benchmark objects are being discovered that offer the chance for detailed study. These include the radio-brightest UCD, NLTT 33370 AB (McLean et al. 2011, Williams et al., in preparation), and the coolest UCD yet detected in the radio, 2MASS J10475385+2124234 (T6.5; Route & Wolszczan 2012; Williams et al. 2013). Wide-field infrared surveys and proper motion searches are discovering substantial numbers of UCDs, including extremely nearby examples such as the 2-pc L/T binary Luhman 16 (Luhman 2013; Burgasser et al. 2013). Finally, theoretical studies of the operation of dynamo action in fully convective bodies are progressing, with numerical geodynamo models being adapted to be able to simulate density contrasts closer to those seen in UCDs (e.g., Christensen et al. 2009). Advances in all of these areas will greatly increase our understanding of the magnetism of brown dwarfs and, eventually, extrasolar planets.

REFERENCES

Alef, W., Benz, A. O., & Güdel, M. 1997, A&A, 317, 707
Antonova, A., Doyle, J. G., Hallinan, G., Golden, A., & Koen, C. 2007, A&A, 472, 257
Antonova, A., Hallinan, G., Doyle, J. G., et al. 2013, A&A, 549, A131
Audard, M., Osten, R. A., Brown, A., et al. 2007, A&A, 471, L63
Baliunas, S. L., Nesme-Ribes, E., Sokoloff, D., & Soon, W. H. 1996, ApJ, 460, 848
Basri, G., & Marcy, G. W. 1995, AJ, 109, 762
Benz, A. O., & Güdel, M. 1994, A&A, 285, 621
Berger, E. 2002, ApJ, 572, 503
—. 2006, ApJ, 648, 629
Berger, E., Ball, S., Becker, K. M., et al. 2001, Nature, 410, 338
Berger, E., Rutledge, R. E., Reid, I. N., et al. 2005, ApJ, 627, 960
Berger, E., Gizis, J. E., Giampapa, M. S., et al. 2008a, ApJ, 673, 1080
Berger, E., Basri, G., Gizis, J. E., et al. 2008b, ApJ, 676, 1307
Berger, E., Rutledge, R. E., Phan-Bao, N., et al. 2009, ApJ, 695, 310
Berger, E., Basri, G., Fleming, T. A., et al. 2010, ApJ, 709, 332
Bower, G., Bolatto, A., Ford, E., & Kalas, P. 2009, ApJ, 701, 1922
Browning, M. K. 2008, ApJ, 676, 1262
Burgasser, A., & Putman, M. 2005, ApJ, 626, 486
Burgasser, A., Sheppard, S., & Luhman, K. L. 2013, ApJ, submitted, arxiv:1303.7283
Carilli, C., & Rawlings, S. 2004, New A Rev., 48, 979
Carson, J. C., Marengo, M., Patten, B. M., et al. 2011, ApJ, 743, 141
Casewell, S. L., Jameson, R. F., & Burleigh, M. R. 2008, MNRAS, 390, 1517
Chabrier, G., & Baraffe, I. 2000, ARA&A, 38, 337
Chabrier, G., & Küker, M. 2006, A&A, 446, 1027
Christensen, U., Holzwarth, V., & Reiners, A. 2009, Nature, 457, 167
Cook, B. A., Williams, P. K. G., & Berger, E. 2013, paired paper 2
Costa, E., Méndez, R., Jao, W. C., et al. 2006, AJ, 132, 1234
Crifo, F., Phan-Bao, N., Delfosse, X., et al. 2005, A&A, 441, 653
Cruz, K., Reid, N., Liebert, J., Kirkpatrick, D., & Lowrance, P. 2003, AJ, 126, 2421
Cruz, K., Reid, N., Kirkpatrick, D., et al. 2007, AJ, 133, 439
Cruz, K. L., & Reid, N. 2002, AJ, 123, 2828
Dahn, C. C., Liebert, J., & Harrington, R. S. 1986, AJ, 91, 621
Deacon, N. R., Hambly, N. C., & Cooke, J. A. 2005, A&A, 435, 363
Delfosse, X., Forveille, T., Perrier, C., & Mayor, M. 1998, A&A, 331, 581
Dennis, B., & Zarro, D. 1993, Solar Physics, 146, 177
Deshpande, R., Martín, E. L., Montgomery, M. M., et al. 2012, AJ, 144, 99
Dobler, W., Stix, M., & Brandenburg, A. 2006, ApJ, 638, 336
Donati, J. F., Morin, J., Petit, P., et al. 2008, MNRAS, 390, 545
Drake, S., Simon, T., & Linsky, J. 1989, ApJS, 71, 905
Dupuy, T., Liu, M., Bowler, B., et al. 2010, ApJ, 721, 1725
Dupuy, T., Liu, M., & Ireland, M. 2009, ApJ, 699, 168
Durney, B. R., de Young, D. S., & Roxburgh, I. W. 1993, Solar Physics, 145, 207
Durney, B. R., Mihalas, D., & Robinson, R. D. 1981, PASP, 93, 537
Faherty, J., Burgasser, A., Cruz, K., et al. 2009, AJ, 137, 1
Fleming, T. A., Giampapa, M. S., & Garza, D. 2003, ApJ, 594, 982
Fleming, T. A., Giampapa, M. S., Schmitt, J. H. M. M., & Bookbinder, J. A. 1993, ApJ, 410, 387
Fomalont, E. B., Windhorst, R. A., Kristian, J. A., & Kellerman, K. I. 1991, AJ, 102, 1258
Forveille, T., Beuzit, J. L., Delorme, P., et al. 2005, A&A, 435, L5
Freed, M., Close, L., & Siegler, N. 2003, ApJ, 584, 453
Freeman, P., Doe, S., & Siemiginowska, A. 2001, Proc. SPIE, 4477, 76

Fruscione, A., McDowell, J., Allen, G., et al. 2006, Proc. SPIE, 6270, 62701V

Gastine, T., Morin, J., Duarte, L., et al. 2013, A&A, 549, L5

Gatewood, G., & Coban, L. 2009, AJ, 137, 402

Gehrels, N. 1986, Astrophys. J., 303, 336

Giampapa, M. S., & Liebert, J. 1986, ApJ, 305, 784

Gizis, J., Monet, D., Reid, N., et al. 2000, AJ, 120, 1085

Gliese, W., & Jahreiß, H. 1991, Preliminary Version of the Third Catalogue of Nearby Stars (Heidelberg: Astron. Rechen-Institut)

Güdel, M., & Benz, A. 1993, ApJ, 405, L63

Güdel, M., Benz, A. O., Schmitt, J. H. M. M., & Skinner, S. L. 1996, ApJ, 471, 1002

Güdel, M., Schmitt, J. H. M. M., Bookbinder, J. A., & Fleming, T. A. 1993, ApJ, 415, 236

Guenther, E. W., & Wuchterl, G. 2003, A&A, 401, 677

Hallinan, G., Antonova, A., Doyle, J. G., et al. 2006, ApJ, 653, 690

—. 2008, ApJ, 684, 644

Harrington, R. S., & Dahn, C. C. 1984, IAU Circ., 3989, 1

Harrington, R. S., Dahn, C. C., & Guetter, H. H. 1974, ApJL, 194, L87

Henry, T. J., Kirkpatrick, J. D., & Simons, D. A. 1994, AJ, 108, 1437

Irwin, J., & Bouvier, J. 2008, Proc. IAU, 4, 363

Jenkins, J. S., Ramsey, L. W., Jones, H. R. A., et al. 2009, ApJ, 704, 975

Kirkpatrick, J. D., Henry, T. J., & McCarthy, D. W. 1991, ApJS, 77, 417

Koen, C. 2013, MNRAS, 428, 2824

Konopacky, Q. M., Ghez, A. M., Barman, T. S., et al. 2010, ApJ, 711, 1087

Konopacky, Q. M., Ghez, A. M., Fabrycky, D. C., et al. 2012, ApJ, 750, 79

Kraft, R., Burrows, D., & Nousek, J. 1991, ApJ, 374, 344

Law, N. M., Hodgkin, S. T., & Mackay, C. D. 2008, MNRAS, 384, 150

Lee, K.-G., Berger, E., & Knapp, G. 2010, ApJ, 708, 1482

Lépine, S., Thorstensen, J., Shara, M., & Rich, M. 2009, AJ, 137, 4109

Liebert, J., Dahn, C. C., Gresham, M., & Strittmatter, P. A. 1979, ApJ, 233, 226

Liu, W., Hu, J. Y., Li, Z. Y., & Cao, L. 1999, ApJS, 122, 257

Lodders, K. 2003, ApJ, 591, 1220

Luhman, K. L. 2013, ApJL, 767, L1

Luyten, W. 1979, New Luyten Catalogue of Stars with Proper Motions Larger than Two Tenths of an Arcsecond (Minneapolis: University of Minnesota Press)

Luyten, W. J. 1976, A Catalogue of 1849 Stars with Proper Motions greater than 0.5″ Annually (Minneapolis: University of Minnesota Press)

Lyubchik, Y., Jones, H. R. A., Pavlenko, Y. V., Pinfield, D. J., & Covey, K. R. 2012, MNRAS, 422, 2195

Martín, E., Delfosse, X., Basri, G., et al. 1999, AJ, 118, 2466

McCarthy, C., & Zuckerman, B. 2004, AJ, 127, 2871

McCarthy, D. W., Henry, T. J., Fleming, T. A., et al. 1988, ApJ, 333, 943

McLean, M., Berger, E., Irwin, J., Forbrich, J., & Reiners, A. 2011, ApJ, 741, 27

McLean, M., Berger, E., & Reiners, A. 2012, ApJ, 746, 23

McMullin, J. P., Waters, B., Schiebel, D., Young, W., & Golap, K. 2007, ASP Conf. Ser., 376, 127

Mohanty, S., & Basri, G. 2003, ApJ, 583, 451

Mohanty, S., Basri, G., Shu, F., Allard, F., & Chabrier, G. 2002, ApJ, 571, 469

Morin, J., Donati, J. F., Petit, P., et al. 2010, MNRAS, 407, 2269

Morin, J., Dormy, E., Schrinner, M., & Donati, J. F. 2011, MNRAS Lett., 418, L133

Morin, J., Donati, J. F., Petit, P., et al. 2008, MNRAS, 390, 567

Nakajima, T., Tsuji, T., & Yanagisawa, K. 2004, ApJ, 607, 499

Nelder, J. A., & Mead, R. 1965, The Computer Journal, 7, 308

Neupert, W. 1968, ApJ, 153, L59

Noyes, R. W., Hartmann, L. W., Baliunas, S. L., Duncan, D. K., & Vaughan, A. H. 1984, ApJ, 279, 763

Offringa, A. R., de Bruyn, A. G., Biehl, M., et al. 2010, MNRAS, 405, 155

Offringa, A. R., van de Gronde, J. J., & Roerdink, J. B. T. M. 2012, A&A, 539, A95

Osten, R., Hawley, S., Allred, J., Johns-Krull, C., & Roark, C. 2005, ApJ, 621, 398

Osten, R., Brown, A., Ayres, T., et al. 2004, ApJS, 153, 317

Osten, R. A., Phan-Bao, N., Hawley, S. L., Reid, I. N., & Ojha, R. 2009, ApJ, 700, 1750

Phan-Bao, N., Osten, R. A., Lim, L., Martín, E. L., & Ho, P. T. P. 2007, ApJ, 658, 553

Phan-Bao, N., Crifo, F., Delfosse, X., et al. 2003, A&A, 401, 959

Pizzolato, N., Maggio, A., Micela, G., Sciortino, S., & Ventura, P. 2003, A&A, 397, 147

Reid, N., Cruz, K., Kirkpatrick, J. D., et al. 2008, AJ, 136, 1290

Reid, N., Hawley, S., & Gizis, J. 1995, AJ, 110, 1838

Reid, N., Cruz, K. L., Laurie, S., et al. 2003, AJ, 125, 354

Rein, H. 2012, A proposal for community driven and decentralized astronomical databases and the Open Exoplanet Catalogue, arxiv:1211.7121

Reiners, A., & Basri, G. 2007, ApJ, 656, 1121

—. 2008, ApJ, 684, 1390

—. 2009, A&A, 496, 787

—. 2010, ApJ, 710, 924

Riaz, B., Gizis, J., & Harvin, J. 2006, AJ, 132, 866

Robrade, J., Poppenhaeger, K., & Schmitt, J. H. M. M. 2010, A&A, 513, A12

Robrade, J., & Schmitt, J. H. M. M. 2005, A&A, 435, 1073

—. 2008, A&A, 487, 1139

Rodono, M., Ciatti, F., & Vittone, A. 1980, AJ, 85, 298

Rojas-Ayala, B., Covey, K., Muirhead, P., & Lloyd, J. 2012, ApJ, 748, 93

Route, M., & Wolszczan, A. 2012, ApJL, 747, L22

Rutledge, R. E., Basri, G., Martín, E. L., & Bildsten, L. 2000, ApJL, 538, L141

Sault, R. J., & Wieringa, M. H. 1994, A&AS, 108, 585

Scargle, J. 1998, ApJ, 504, 405

Scargle, J., Norris, J., Jackson, B., & Chiang, J. 2013, ApJ, 764, 167

Schmidt, S., Cruz, K., Bongiorno, B., Liebert, J., & Reid, N. 2007, AJ, 2258

Schmitt, J., Fleming, T., & Giampapa, M. 1995, ApJ, 450, 392

Schmitt, J. H. M. M., & Liefke, C. 2002, A&A, 382, L9

—. 2004, A&A, 417, 651

Semel, M. 1989, A&A, 225, 456

Siegler, N., Close, L., Cruz, K., Martín, E., & Reid, N. 2005, ApJ, 621, 1023

Skrutskie, M. F., Cutri, R. M., Stiening, R., et al. 2006, AJ, 131, 1163

Smith, R., Brickhouse, N., Liedahl, D., & Raymond, J. 2001, ApJL, 556, L91

Stelzer, B. 2004, ApJL, 615, L153

Stelzer, B., Micela, G., Flaccomio, E., Neuhäuser, R., & Jayawardhana, R. 2006a, A&A, 448, 293

Stelzer, B., Schmitt, J. H. M. M., Micela, G., & Liefke, C. 2006b, A&A, 460, L35

Stelzer, B., Alcalá, J., Biazzo, K., et al. 2012, A&A, 537, A94

Treumann, R. 2006, A&A Rev., 13, 229

van Altena, W. F., Lee, J. T., & Hoffleit, E. D. 1995, The general catalogue of trigonometric parallaxes (New Haven: Yale University Observatory)

VanderPlas, J., Connolly, A., Ivezic, Z., & Gray, A. 2012, in 2012 Conference on Intelligent Data Understanding (IEEE), 47

Vaughan, A. H., & Preston, G. W. 1980, PASP, 92, 385

Vilhu, O. 1984, A&A, 133, 117

Voges, W., Aschenbach, B., Boller, T., et al. 1999, A&A, 349, 389

West, A., & Basri, G. 2009, ApJ, 693, 1283

West, A. A., Hawley, S. L., Walkowicz, L. M., et al. 2004, AJ, 128, 426

White, S., Jackson, P., & Kundu, M. 1989, Astrophys. J. Supp., 71, 895

Wilking, B., Greene, T., & Meyer, M. 1999, AJ, 117, 469

Williams, P., Berger, E., & Zauderer, A. 2013, ApJL, 767, L30

Williams, P. K. G., et al. 2013, in preparation

Wright, N., Drake, J., Mamajek, E., & Henry, G. 2011, ApJ, 743, 48

Wu, C. S., & Lee, L. C. 1979, ApJ, 230, 621

Zapatero Osorio, M. R., Lane, B. F., Pavlenko, Y., et al. 2004, ApJ, 615, 958

Zapatero Osorio, M. R., Martín, E. L., Bouy, H., et al. 2006, ApJ, 647, 1405

Zarka, P. 1998, JGR, 103, 20159

APPENDIX

Here we give our method for computing bolometric luminosities and discuss the properties of the sources for which we present new results.

Bolometric luminosities

We compute bolometric luminosities using bolometric corrections to observed absolute magnitudes. In particular,

$$[L_{\rm bol}] = \frac{2}{5}(M_{\odot,\rm bol} - M - {\rm BC}) + [L_{\odot}], \tag{1}$$

where M is the absolute magnitude of the star in some band, BC is the bolometric correction in that band, and $M_{\odot,\rm bol} = 4.7554$ is the bolometric absolute magnitude of the Sun. For M dwarfs, we use the average of the bolometric luminosities calculated using J and K band magnitudes:

$$ {\rm BC}_K = 2.43 + 0.0895 \times ({\rm SP}) \tag{2}$$

and

$$ {\rm BC}_J = 1.53 + 0.148 \times ({\rm SP}) - 0.0105 \times ({\rm SP})^2, \tag{3}$$

with SP $= 0$ (5) for spectral type M0 (M5) (Wilking et al. 1999). For L dwarfs, we use the K-band magnitude only:

$$ {\rm BC}_K = \begin{cases} 2.37 + 0.075 \times ({\rm SP}), & 10 \leq {\rm SP} < 14, \\ 4.47 - 0.075 \times ({\rm SP}), & 14 \leq {\rm SP} \leq 19, \end{cases} \tag{4}$$

with SP used consistently as above (SP $= 10$ for L0) (Nakajima et al. 2004).

Properties of Newly-Observed Targets

LHS 292

LHS 292 (= GJ 3622, LP 731–58) is a nearby ($d \approx 4.5$ pc) M6.5 dwarf. It is a variable Hα emitter with $[L_{\rm H\alpha}/L_{\rm bol}] \approx -4.4$ (Dahn et al. 1986; Lee et al. 2010; Reiners & Basri 2010) and has been suggested as a candidate UV Cet flare star (Dahn et al. 1986). K-band spectroscopy and modeling yield an estimated $T_{\rm eff} = 2772 \pm 25$ K and $[{\rm Fe/H}] = -0.41 \pm 0.17$ (Rojas-Ayala et al. 2012). Reiners & Basri (2010) used other spectroscopic measurements to determine $v \sin i < 3 \pm 2$ km s^{-1} and $Bf = 600 \pm 200$ G, where Bf is the magnetic field average on the visible surface with filling factor $f \leq 1$. ROSAT observations by Fleming et al. (1993) yielded an upper limit of $[L_{\rm X}] < 26.42$ in the 0.1–2.4 keV band. McLean et al. (2012) observed LHS 292 in the radio and did not detect it, obtaining a limit of $S_\nu < 96$ μJy ($[L_{\rm R}/L_{\rm bol}] < -8.20$) at 8.46 GHz. Morin et al. (2010) used Zeeman-Doppler imaging to derive a low-resolution map of the stellar magnetic field structure. Although the S/N was low, their modeling indicates a dipolar field of $\sim$100 G with an inclination $i \approx 60°$. From variability in its radial velocity on the 10 km s^{-1} level, Guenther & Wuchterl (2003) argue that LHS 292 is a binary system, but a companion has not yet been detected by other means.

LHS 523

LHS 523 (= GJ 4281, LP 760–3) is an M6.5 dwarf at a distance of 11 pc. Giampapa & Liebert (1986) measured its Hα EW to be 1.3 Å. Mohanty & Basri (2003) measure an Hα EW of 4.4 Å ($[L_{\rm H\alpha}/L_{\rm bol}] = -4.15$) and $v \sin i = 7.0$ km s^{-1}, consistent with a later determination of $v \sin i < 12$ km s^{-1} using a different method (Lyubchik et al. 2012). A proper motion of 1200 ± 130 mas yr^{-1} has been determined (Deacon et al. 2005). Jenkins et al. (2009) determine $T_{\rm eff} = 2536$ K and $M = 0.093 \pm 0.005$ M$_\odot$ from photometric modeling. LHS 523 was undetected in a ROSAT survey of very-low-mass stars (Fleming et al. 1993), with $[L_{\rm X}] < 26.89$.

LHS 2397a AB

LHS 2397a AB (= GJ 3655, LP 732–94) is an M8+L7.5 binary at a distance of 14 pc. The brown dwarf companion was detected by direct imaging with adaptive optics by Freed et al. (2003). Long-term monitoring has led to a detailed model of the binary orbit (Dupuy et al. 2009; Konopacky et al. 2010), with the total system mass being estimated as 0.144 ± 0.013 M$_\odot$ (Konopacky et al. 2010). The projected rotational velocities of the primary and secondary have been measured as $v \sin i = 15 \pm 1$ and 11 ± 3, respectively (Konopacky et al. 2012). Mohanty & Basri (2003) detected strong Hα emission with EW = 29.4 Å, computing $[L_{\rm H\alpha}/L_{\rm bol}] = -3.70$. Comparable results were obtained by Schmidt et al. (2007), who found even stronger emission with $[L_{\rm H\alpha}/L_{\rm bol}] = -3.40$, making it one of the most Hα-luminous UCDs known.

LHS 3406

LHS 3406 (= V492 Lyr, GJ 4073, LP 229–30) is an M8 dwarf at a distance of 14 pc. In an investigation of candidate cataclysmic variable systems, Liu et al. (1999) confirmed its dMe nature and measured $[L_{H\alpha}/L_{bol}] \approx -4.1$. Subsequent activity observations by Schmidt et al. (2007) find $[L_{H\alpha}/L_{bol}] \approx -4.3$. High-resolution spectra obtained by Reiners & Basri (2010) reveal a rotational velocity of $v \sin i = 5.0 \pm 3.2$ km s^{-1}, $[L_{H\alpha}/L_{bol}] = -4.1$, and $Bf = 1200 \pm 800$ G. This is consistent with the results of Deshpande et al. (2012), who find $v \sin i < 12$ km s^{-1}. Previous radio observations with the VLA yielded an upper limit of $S_\nu < 48$ μJy at 8.46 GHz (Berger 2006). LHS 3406 was undetected in the ROSAT survey of Fleming et al. (1993) with an upper limit of $[L_X] < 26.83$. In a search for brown dwarf companions, no objects were found within limits of $\Delta J < 9.6$, $\Delta \theta > 10''$ (McCarthy & Zuckerman 2004).

LP 647–13

LP 647–13 (= NLTT 3868) is an M9 dwarf at a distance of 11 pc. In the survey of Schmidt et al. (2007), it was found that $[L_{H\alpha}/L_{bol}] \approx -4.5$. Reiners & Basri (2010) found a rotational velocity of $v \sin i = 13 \pm 2$ km s^{-1} as well as $[L_{H\alpha}/L_{bol}] = -4.50$ and $Bf = 1400 \pm 200$ G. Deshpande et al. (2012) obtain consistent results, with $v \sin i < 12$ km s^{-1}. Radio observations with the VLA have yielded an upper limit of $S_\nu < 33$ μJy at 8.46 GHz (Berger 2006).

LP 851–346

LP 851–346 (= DENIS-P J115542.9−222458) is an M7.5 dwarf at a distance of 9.7 pc. Despite the fact that it has been suspected to be a very nearby object for nearly 40 years (Luyten 1976), it is poorly-studied. Reiners & Basri (2010) found a rotational velocity of $v \sin i = 33 \pm 3$ km s^{-1} and $[L_{H\alpha}/L_{bol}] = -4.58$. Radio observations with the VLA have yielded an upper limit of $S_\nu < 90$ μJy at 8.46 GHz (McLean et al. 2012).

NLTT 40026

NLTT 40026 (= LSPM J1521+5053) is an M7.5 dwarf at a distance of 16.1 pc. Schmidt et al. (2007) measured $[L_{H\alpha}/L_{bol}] \approx -4.9$. Reiners & Basri (2010) measured $v \sin i = 40 \pm 4$ km s^{-1} and $[L_{H\alpha}/L_{bol}] = -4.88$. Radio observations with the VLA have yielded an upper limit of $S_\nu < 39$ μJy at 8.46 GHz (Berger 2006). Siegler et al. (2005) found no evidence for any companions to NLTT 40026 between 0.1–15 arcsec with a separation-dependent contrast of $\Delta H \lesssim 12$ mag.

Properties of Targets with New Analysis

G 208-44AB/45

The G 208-44AB/45 system (= GJ 1245 ABC) is a well-studied, nearby (4.6 pc), cool triple (McCarthy et al. 1988). G 208–44 AB (= GJ 1245 AC, LHS 3494 AB, LSPM J1953+4424W) is separated from G 208–45 (= GJ 1245 B, LHS 3495, LSPM J1953+4424E) by $\sim$7$''$, and is itself a tighter binary of $\sim$1$''$ separation. Both components of the overall system are flare stars (Rodono et al. 1980) and it has long been a target of activity studies (e.g., White et al. 1989). The blended pair G 208–44 AB has a radio flux density <192 μJy at 5 GHz (Bower et al. 2009), $[L_X/L_{bol}] \approx -3.78$ (Schmitt et al. 1995), $[L_{H\alpha}/L_{bol}] \approx -4.3$ (Mohanty & Basri 2003), and $v \sin i = 17.4 \pm 1.4$ km s^{-1} (Delfosse et al. 1998). Resolved measurements of G 208–44 AB are uncommon, with Law et al. (2008) recently providing the first spectral type estimate for G 208–44 B (M8.5); it is the only component of the system that fits our definition of being an ultracool dwarf. Mohanty & Basri (2003) were able to measure $v \sin i$ in G 208–44 A (22.5 ± 2 km s^{-1}) and G 208–45 (6.8 ± 1.9 km s^{-1}), but not G 208–44 B.

DENIS 0255−4700

DENIS-P J025503.3−470049 (= 2MUCD 10158; hereafter DENIS 0255−4700), an L8 dwarf at a distance of 5 pc, was identified as an extremely cool object by Martín et al. (1999), with $T_{eff} \approx 1500$ K (Reiners & Basri 2008). Its Hα emission is extremely faint, $[L_{H\alpha}/L_{bol}] < -8.28$ (Reiners & Basri 2008). Multiple measurements of its $v \sin i$ yield either $\sim$40 or $\sim$60 km s^{-1}, depending on the analysis method used, likely due to its unusually late type (Mohanty & Basri 2003; Zapatero Osorio et al. 2006; Reiners & Basri 2008). Brown dwarf companions with separations of $\sim$7–165$''$ are unlikely (Carson et al. 2011). Optical monitoring suggests short- and long-term aperiodic variations (Koen 2013).

LP 349–25 AB

LP 349–25 AB (= LSPM J0027+2219, NLTT 1470) is an M8+M9 binary at a distance of $\sim$10 pc. Gizis et al. (2000) found moderate Hα activity in the blended system, with $[L_{H\alpha}/L_{bol}] = -4.52$. Forveille et al. (2005) used adaptive-optics imaging to reveal the binarity of the system, finding a separation of $\sim$0.1$''$ with $\Delta K' = 0.26 \pm 0.05$ mag. A measurement of the trigonometric parallax, $\pi = 75.82 \pm 1.62$ mas, has only recently become available (Gatewood & Coban 2009). Reiners & Basri (2010) found $[L_{H\alpha}/L_{bol}] = -4.53$, in very good agreement with Gizis et al. (2000), but were unable to assess the magnetic field strength. Phan-Bao et al. (2007) discovered radio emission from the system with a flux density at 8.5 GHz of 365 ± 16 μJy. Both of the components are rapid rotators, although their projected rotational velocities differ by $\sim$15%: $v \sin i = 55 \pm 2$ km s^{-1} and 83 ± 3 km s^{-1} for the A and B components, respectively (Konopacky et al. 2012). The total mass of the system is $0.120^{+0.008}_{-0.007}$ $M_\odot$ and it is also likely to be young, at 140 ± 30 Myr (Dupuy et al. 2010).

Table 8
Radio and X-ray Data for UCDs

2MASS Identifier	SpT	$[L_{\rm bol}]$ $[L_\odot]$	St.	X-Ray Band (keV)	$[L_X]$ [erg s^{-1}]	$[L_{\nu,R}]$ [erg s^{-1} Hz^{-1}]	$[L_X/L_{\rm bol}]$	$[L_{\nu,R}/L_{\rm bol}]$ [Hz^{-1}]	$[L_{\nu,R}/L_X]$ [Hz^{-1}]	Ref. (X)	Ref. (R)
(1)	(2)	(3)	(4)	(5)	(6)	(7)	(8)	(9)	(10)	(X)	(R)
10481258−1120082	M6.5	−3.15	–	0.2–2.0	25.7	< 11.8	−4.7	< −18.7	< −13.9	⋆	⋆
22285440−1325178	M6.5	−3.13	–	0.2–2.0	25.7	< 12.3	−4.8	< −18.1	< −13.4	⋆	⋆
¶13142039+1320011 AB	M7	−2.40	Q	0.2–2.0	27.6	14.7	−3.6	−16.5	−12.9	5	5
¶			F	0.2–2.0	28.3	14.7	−2.9	−16.5	−13.7	5	5
14563831−2809473	M7	−3.29	–	0.1–2.4	26.2	13.1	−4.1	−17.2	−13.1	7	8
16553529−0823401	M7	−3.21	–	0.1–2.4	26.9	< 12.7	−3.5	< −17.7	< −14.2	10	10
11554286−2224586	M7.5	−3.32	Q	0.2–2.0	25.8	< 12.3	−4.4	< −17.9	< −13.5	⋆	⋆
			F	0.2–2.0	26.7	< 12.3	−3.5	< −17.9	< −14.4	⋆	⋆
15210103+5053230	M7.5	−3.30	–	0.2–2.0	25.7	< 12.7	−4.6	< −17.6	< −13.0	⋆	⋆
00275592+2219328 AB	M8	−2.93	Q	0.2–2.0	25.8	13.8	−4.8	−16.8	−12.0	⋆	8
			F	0.2–2.0	26.3	13.8	−4.3	−16.8	−12.5	⋆	8
03205965+1854233	M8	−3.29	Q	0.3–8.0	27.2	< 13.3	−3.1	< −17.0	< −13.9	14	8
			F	0.3–8.0	29.7	< 13.3	−0.6	< −17.0	< −16.4	14	8
11214924−1313084 AB	M8	−3.36	–	0.2–2.0	27.1	13.2	−3.1	−17.0	−13.9	⋆	⋆
18432213+4040209	M8	−3.16	Q	0.2–2.0	26.5	< 12.6	−3.9	< −17.8	< −13.9	⋆	⋆
			F	0.2–2.0	27.1	< 12.6	−3.4	< −17.8	< −14.5	⋆	⋆
19165762+0509021	M8	−3.30	Q	0.2–2.0	25.2	< 12.6	−5.1	< −17.7	< −12.7	16	8
			F	0.2–2.0	25.7	< 12.6	−4.6	< −17.7	< −13.2	16	8
14542923+1606039 Bab	M8.5	−3.17	Q	0.5–8.0	25.9	< 13.7	−4.5	< −16.8	< −12.2	19	8
			F	0.5–8.0	27.6	< 13.7	−2.8	< −16.8	< −13.9	19	8
¶18353790+3259545	M8.5	−3.52	–	0.2–2.0	< 24.5	13.3	< −5.6	−16.8	> −11.3	16	16
01095117−0343264	M9	−3.48	Q	0.2–2.0	25.2	< 12.5	−4.9	< −17.6	< −12.7	⋆	⋆
			F	0.2–2.0	26.1	< 12.5	−4.0	< −17.6	< −13.5	⋆	⋆
03393521−3525440	M9	−3.81	Q	0.1–10.0	< 24.0	12.3	< −5.7	−17.4	> −11.7	20	8
			F	0.1–10.0	25.6	13.9	−4.2	−15.9	−11.7	20	8
08533619−0329321	M9	−3.52	Q	0.3–0.8	26.5	< 12.8	−3.5	< −17.2	< −13.7	21	22
			F	0.1–2.4	27.6	< 12.8	−2.5	< −17.2	< −14.8	23	22
10481463−3956062	M9	−3.54	–	0.2–2.0	25.1	12.4	−4.9	−17.6	−12.7	26	8
14284323+3310391	M9	−3.63	–	0.1–2.4	< 25.5	< 13.1	< −4.4	< −16.9		27	8
¶15010818+2250020	M9	−3.67	Q	0.3–2.0	24.9	13.4	−5.0	−16.5	−11.5	28	28
¶			F	0.3–2.0	27.3	14.5	−2.6	−15.4	−12.8	28	28
¶00242463−0158201	M9.5	−3.49	–	0.2–2.0	< 25.1	< 12.9	< −4.9	< −17.2		30	30
00274197+0503417	M9.5	−3.67	–	0.3–8.0	< 26.2	< 14.7	< −3.7	< −15.2		26	22
¶07464256+2000321 AB	L0	−3.36	Q	0.2–2.0	< 25.2	13.6	< −5.0	−16.6	> −11.6	31	31
			F	0.2–2.0	< 25.2	15.4	< −5.0	−14.8	> −9.8	31	8
¶06023045+3910592	L1	−3.67	–	0.2–2.0	< 25.0	< 12.8	< −4.9	< −17.2		30	30
¶13054019−2541059 AB	L2	−3.56	–	0.1–10.0	25.3	< 12.8	−4.7	< −17.3	< −12.6	32	32
¶05233822−1403022	L2.5	−3.82	–	0.2–2.0	< 25.2	< 12.9	< −4.5	< −16.8		30	30
¶00361617+1821104	L3.5	−3.99	Q	0.2–8.0	< 24.9	13.4	< −4.7	−16.2	> −11.6	33	33
			F	0.2–8.0	< 24.9	13.8	< −4.7	−15.8	> −11.1	33	22
12281523−1547342 AB	L5	−3.93	–	0.3–8.0	< 26.6	< 13.6	< −3.0	< −16.0		26	22
15074769−1627386	L5	−4.23	–	0.2–8.0	< 24.8	< 12.6	< −4.6	< −16.8		33	22

References. — Columns are (X), X-ray flux; (R), radio flux. [⋆]: this work, [1] Henry et al. (1994), [2] van Altena et al. (1995), [3] Kirkpatrick et al. (1991), [4] Lépine et al. (2009), [5] Williams et al. (2013, in preparation), [6] Cruz et al. (2003), [7] Schmitt et al. (1995), [8] McLean et al. (2012), [9] Gliese & Jahreiß (1991), [10] Güdel et al. (1993), [11] Crifo et al. (2005), [12] Gatewood & Coban (2009), [13] Cruz et al. (2007), [14] Stelzer et al. (2006b), [15] Freed et al. (2003), [16] Berger et al. (2008b), [17] Zapatero Osorio et al. (2004), [18] Stelzer (2004), [19] Stelzer et al. (2006a), [20] Rutledge et al. (2000), [21] Robrade & Schmitt (2008), [22] Berger (2002), [23] Schmitt & Liefke (2002), [24] Reiners & Basri (2010), [25] Reid et al. (2008), [26] Stelzer et al. (2012), [27] Fleming et al. (1993), [28] Berger et al. (2008a), [29] Reid et al. (1995), [30] Berger et al. (2010), [31] Berger et al. (2009), [32] Audard et al. (2007), [33] Berger et al. (2005)

Note. — Rows marked with a pilcrow (¶) indicate simultaneous radio and X-ray observations. Col. (4) is the state of the source: quiescent (Q), flaring (F), or indeterminate/unknown (–). $[L_{\rm X}]$ has been normalized to the 0.2–2 keV bandpass as described in the text.